Open access • Journal Article • DOI:10.1002/ADMA.201804903

Hollow Functional Materials Derived from Metal-Organic Frameworks: Synthetic Strategies, Conversion Mechanisms, and Electrochemical Applications.

Ze-Xing Cai, Zhongli Wang, Jeonghun Kim, Jeonghun Kim ...+1 more authors

Institutions: National Institute for Materials Science, Qingdao University of Science and Technology, University of Queensland

Published on: 01 Mar 2019 - Advanced Materials (John Wiley & Sons, Ltd)

DOI:10.1002/adma.201804903

Article Type: Review

Hollow Functional Materials Derived from Metal–Organic Frameworks: Synthetic Strategies, Conversion Mechanisms and Electrochemical Applications

Ze-Xing Cai, Zhong-Li Wang,* Jeonghun Kim, Yusuke Yamauchi*

Z.-X. Cai, Z.-L. Wang, Y. Yamauchi
International Center for Materials Nanoarchitectonics (MANA), National Institute for Materials Science (NIMS)
1-1 Namiki, Tsukuba, Ibaraki 305-0044, Japan

E-mail: WANG.Zhongli@nims.go.jp

J. Kim, Y. Yamauchi
School of Chemical Engineering and Australian Institute for Bioengineering and Nanotechnology (AIBN), The University of Queensland
Brisbane, QLD 4072, Australia
E-mail: y.yamauchi@uq.edu.au

Keywords: batteries, conversion mechanisms, electrocatalysis, hollow structures, metal–organic frameworks

Hollow materials derived from metal–organic frameworks (MOFs), by virtue of their controllable configuration, composition, porosity, and specific surface area, have shown fascinating physicochemical properties and widespread applications, especially in electrochemical energy storage and conversion. Here, the recent advances in the controllable synthesis are discussed, mainly focusing on the conversion mechanisms from MOFs to hollow-structured materials. The synthetic strategies of MOF-derived hollow-structured materials are broadly sorted into two categories: the controllable synthesis of hollow MOFs and subsequent pyrolysis into functional materials, and the controllable conversion of solid MOFs with predesigned composition and morphology into hollow structures. Based on the formation processes of hollow MOFs and the conversion processes of solid MOFs, the synthetic strategies are further conceptually grouped into six categories: template-mediated assembly, stepped dissolution–regrowth, selective chemical etching, interfacial ion exchange, heterogeneous construction, and self-catalytic pyrolysis. By analyzing and discussing fourteen types of reaction processes in detail, a systematic mechanism of conversion from MOFs to hollow-structured materials is exhibited. Afterward, the applications of these hollow structures as electrode materials for lithium-ion batteries, hybrid supercapacitors, and electrocatalysis are presented. Finally, an outlook on the emergent challenges and future developments in terms of their controllable fabrications and electrochemical applications is further discussed.

1. Introduction

The physical/chemical properties of materials are governed by the synergistic effects of structures and compositions. The unique structure of hollow-structured materials provides various advantageous features: enhanced surface-to-volume ratio, low density, microreactor environment, higher loading capacities, and reduced transmission lengths of mass and charge. Therefore, hollow-structured materials have attracted significant attention with regard to future technological applications, such as electrochemical energy storage,[1-3] photocatalysis/electrocatalysis,[4, 5] medicine carriers,[6, 7] chemical adsorbents,[8-10] and sensing technologies.[11, 12] The preparation of hollow structures has long been a popular research field. As recently as the last century, hollow-structured materials could only be controllably synthesized and regulated on the macro- and microscale by using methods such as spray-drying and gas-blowing.[13] Until 1998, Caruso synthesized and engineered hollow-structured silica and silica–polymer hybrid spheres by using a colloid as a template and promoted the development of various hollow nanostructure fabrications based on the template method by constructing shells with different chemical compositions.[14] Template methods have long been a versatile synthesis paradigm for hollow structures because of their advantages in the control of hollow structures with essentially any dimension, configuration, and chemistry. More recently, numerous physical and chemical strategies have been investigated with a view toward synthesizing hollow-structured materials, such as templated-assisted assembly,[15] self-assembly,[16] chemical etching,[17, 18] galvanic replacement,[19, 20] Oswald ripening,[21] and Kerkendal diffusion.[22] Although great achievements have been made, however, the synthesis of porous/hollow-structured materials with controllable structures (especially complex structures) and certain composition in a controlled manner is

still not an easy task. There are strong future demands to synthesize hollow-structured materials for various technological applications.

Metal–organic frameworks (MOFs), coordination networks with organic ligands containing potential voids, have become a rapidly expanding research area in the last two decades.[23-26] To date, more than 20 000 different MOFs have been fabricated and characterized, thanks to their numerous varieties of primary building blocks and potential for flexible rational design. Due to their unique structural characteristics, such as uniform pore structures, atomic-level structural uniformity, tunable porosity, extensive varieties, and flexibilities in network topology, geometry, dimension, and chemical functionality, MOFs have received widespread attention for a variety of applications in many fields, such as gas storage and separation, liquid separation and purification, electrochemical energy storage, catalysis, and sensing.[27-39] In addition to direct applications, MOFs have been highlighted in recent years as unique precursors for the construction of inorganic functional materials with unrivaled design possibilities, such as carbons, metal-based compounds, and their composites.[40-42] Typically, the morphologies of MOFs are well preserved during the thermal transformation, and controlling the growth of the precursor MOFs has enabled various carbon materials to be fabricated, such as one-dimensional (1D) carbon nanorods, 2D graphene nanoribbons, and 3D hierarchical porous carbons.[43-46] Compared with other conventional solid precursors, these MOF-derived materials possess advantageous features such as high surface areas, ordered multilevel porosities, and designable functionalities that ensure their good performances as functional materials.[47, 48] Remarkably, the unique advantages of MOFs as precursors are fully reflected in the synthesis of hollow-structured materials. Due to their distinct porous structures and tailored chemical constitution, MOFs enable the fabrication of hollow

nanostructures in a controllable manner. To date, various strategies have been developed to synthesize hollow materials from MOFs, such as template-mediated assembly, interfacial synthesis, chemical etching, ion-exchange reactions, and thermal treatments.[49-52] MOF-derived hollow architectures have plentiful variations in structural complexity, such as tunable porosity, diverse morphology, hierarchical/multishelled structures, and multiple internal chambers/channels, which largely enhance their intrinsic applications, especially, bringing great advantages to electrochemical energy-related technologies.

Due to their excellent electrochemical performances, MOF-derived hollow materials have received tremendous attention in recent years.[53-55] Although several reviews have been published on MOF-derived hollow materials, these papers mainly focus on the synthetic methods, complex nanostructures, and electrochemical applications.[56, 57] However, one of the important aspects has been neglected: the conversion mechanisms from MOFs to hollow-structured materials. This is a very difficult topic because it involves complex reaction mechanisms, but it is really important for further design and synthesis of novel hollow structures in a more controllable manner. Based on this point, we analyze and discuss the formation processes of hollow MOFs and conversion processes of solid MOFs based on six synthetic strategies and focus on the reaction mechanisms involved in each synthetic strategy with a total of fourteen. According to the features of MOF precursors, the synthesis strategies are broadly divided into two categories: the controllable synthesis of hollow MOFs and subsequent pyrolysis into functional materials, and the controllable conversion of solid MOFs with predesigned composition and morphology into hollow structures. Based on the formation processes of hollow MOFs and conversion processes of solid MOFs, the synthetic strategies are further conceptually grouped into six categories: template-mediated assembly,

stepped dissolution–regrowth, selective chemical etching, interfacial ion exchange, heterogeneous construction, and self-catalytic pyrolysis. Each strategy contains at least two types of reactions. By analyzing and discussing fourteen types of reaction processes in detail, we exhibit for the first time a systematic conversion mechanism from MOFs to hollow-structured materials. In addition, their electrochemical applications as electrode materials or catalysts for LIBs, SCs, water splitting, and fuel cells are further discussed. Finally, we conclude with some personal insights into the present challenges and future directions in this fascinating research field.

2. Synthetic Strategies and Conversion Mechanisms of MOF-Derived Hollow Architectures

2.1. Controllable Synthesis of Hollow MOFs and Subsequent Pyrolysis into Hollow Materials

Various fabrication strategies have been developed to synthesize hollow MOF nanoarchitectures,[58] including template-mediated assembly,[59-61] stepped dissolution–regrowth,[62-67] and selective chemical etching.[68-72] Subsequently, their corresponding hollow target products, such as nanoporous carbon, metal-based compounds, and their composites, can generally be obtained by careful pyrolysis of hollow MOF precursors in a specific atmosphere at a suitable temperature. A brief introduction of the formation mechanisms in each fabrication strategy is given below.

2.1.1. Template-Mediated Assembly

The template-mediated strategy, which uses removable or expendable templates, is believed to be the most straightforward method for the synthesis of hollow-structured materials.[73, 74] Through a typical template-mediated method, hollow architectures can be synthesized by a multi-step process, including the preparation of a core@shell hybrid intermediate using an external template, followed by the morphology-preserved transformation and removal of templates (if necessary). Due to the inherited shapes of the templates, the most obvious advantage of the template-mediated strategy is the easy control of the size and morphology of the hollow products achieved by using different templates and tuning the coating procedure. Additionally, the compositions and hollow structures of the products can be effectively constructed and tailored by selecting appropriate framework building blocks (i.e., metal nodes and polyfunctional organic linkers) or introducing other co-template/functional materials. It is important to prepare nanostructures with controlled morphologies, chemical compositions, and hierarchical structures, which are essential for good performance as electrode materials and electrocatalysts due to the effects on transfer processes of charge and mass. In general, a vast array of materials can be applied as templates to synthesize hollow MOFs, such as polystyrene, silica, metal oxides, surfactants, double-layered hydroxide, and oil droplets. According to the properties of the templates, the developed template approaches can be divided into two categories: nonreactive template-induced assembly and reactive template-induced assembly. Based on the combination type between template core and MOF shell, the former category can be subdivided into surface coordination-induced assembly and electrostatic interaction-induced assembly, and the latter can be further subdivided into solid–liquid interfacial reaction-induced assembly and liquid–liquid interfacial reaction-induced assembly.

The surface coordination-induced assembly strategy was developed and applied mostly in hard template cases, typically polystyrene (PS), silica, and metal oxides.[59, 74-82] This strategy relies mainly on the coordination interactions between the surface functional groups and metal nodes, which initiate the uniform coating of a layer of the MOF nucleus on the surfaces of templates under an optimized condition. Therefore, modification of the solid templates with functional groups, such as carboxy/sulfone groups and poly(vinylpyrrolidone) (PVP), is necessary. As an example, Tian et al. recently demonstrated the controlled synthesis of a hollow 1D MoO_2/carbon composite using a template@MOF composite-assisted method as shown in **Figure 1**a.[80] Amphiphilic PVP was first used to adsorb onto the surface of MoO_3 nanorods to form PVP-modified MoO_3 composite nanorods. The modification of PVP can enhance the affinity of MoO_3 nanorods to MOF precursors through weak coordination interactions between the amide carbonyl groups and metal ions in solution,[81] which initiates the uniform growth of a layer of bimetallic zeolitic imidazolate frameworks (BMZIFs) on the surface of the MoO_3 nanorods. In contrast, without the pre-modification, the MOF shell could not grow well on the template surfaces of and would overgrow away with the reaction time increasing (Figure 1d). During the subsequent controlled annealing process, the MoO_3@BMZIFs core–shell-structured composites were spontaneously converted into porous carbon-coated MoO_2 composites, as a result of the thermal pyrolysis of the BMZIFs shell and the simultaneous reduction of MoO_3 by carbon. Then the inner MoO_2 core is dissolved and dispersed into the porous carbon matrix by treatment with hot, concentrated HCl, resulting in the formation of a hollow-nanotube structure, as shown in Figure 1e. The as-prepared hollow MoO_2/carbon nanotubes possess typical structural features of improved pore structure and degree of graphitization. Among the templates for surface coordination-induced assembly,

there is a special one: the MOF itself can also be used as a template. The terminated suspended ligands or incompletely coordinated metal nodes on the surface of the MOF crystal can act as unique functional groups to induce the growth of another MOF shell.[83-87] Meanwhile, the formation of core–shell-structured MOFs relies on the close lattice mismatch between the MOF core and the MOF shell.[88] The core–shell MOFs can be controllably converted into hollow MOFs by selectively dissolving the MOF core based on the different chemical stability of the MOF core and shell.[89-94]

The electrostatic interaction-induced assembly generally involves MOF precursors being attracted to the surface of the template under the effect of electrostatic adsorption and then self-assembling into a crystalline shell. The charged template and the formation of counterions from the MOF precursors are premises for this strategy. As an example, Zeng's group reported the application of a micellar of ionic surfactant (alkyltrimethylammonium bromide, C_nTAB, n = 12, 14, 16) as a template for the fabrication of highly uniform ZIF-67 hollow spheres (Figure 1f–h).[95] A certain concentration of C_nTAB will form micelles with hydrophobic chains stacked in a bilayer structure in the solution under a thermodynamic equilibrium condition. The C_nTAB micellar assemblages are positively charged due to the ionization of bromide ions. In the ZIF-67 precursor solution, a tetrahedral coordinated Co^{2+} complex (e.g., [Co(HmIM)(mIM)(L_2)], where L represents mIM^- and auxiliary charged ligands (Br^-, NO_3^-)) are present during the assembly of the crystalline ZIF-67 framework. When C_nTAB and $Co(NO_3)_2$ are mixed with an aqueous HmIM solution, before oligomerization takes place, the two counterions will attract each other and form vesicles consisting of CTA^+, [Co-complex]$^-$, NO_3^-, and Br^- under electrostatic interaction, behaving as the combination of Class II Hofmeister anions and cationic surfactants.[98] Subsequently,

[Co-complex]$^{-}$ species clustering on the surface of the vesicles serve as nucleation sites for the heterogeneous epitaxial growth of ZIF-67 crystals into a polycrystalline shell. The final product is obtained after post-synthetic washing using organic solvents to remove the interior soft template. Remarkably, this synthetic approach can applicable to other classes of hollow MOFs, such as HKUST-1[99] and Co-BTB[100] (where BTB is 1,3,5-tris(4-carboxyphenyl)benzene).

The solid–liquid interfacial reaction-induced assembly refers to the application of certain insoluble solid reactants with specific structures both as templates and precursors in the formation process of hollow superstructures. Generally, most MOF crystals are prepared via coordination reactions between soluble metal salts and organic ligands in a homogeneous solution. Alternatively, in recent years, solid metal-containing materials (metals, metal oxides, hydroxides, carbonates, etc.) have been developed as templates and precursors for directing the formation of MOFs.[101, 102] When these solid matters are dispersed in a solution of organic ligand, they are insoluble in the solvent but they can react slowly with the organic ligands at the solid–liquid interface through nucleation, growth, and self-assembly into the MOF shell. By carefully designing appropriate template components and controlling the reaction process, core–shell structures of template@MOFs can be synthesized. For example, For example, Chen et al. reported the synthesis of uniform polymer-$Co(Ac)_2$@ZIF-67 composite nanofibers by dispersing cobalt acetate ($Co(Ac)_2$) in a polyacrylonitrile (PAN) polymer and conducting a partial phase transformation of the composite nanofibers with 2-methylimidazole in ethanol.[96] Then, the remaining template core can be dissolved in DMF, resulting in tubular ZIF-67. Hierarchical CNT/Co_3O_4 composite microtubes are finally fabricated through heat treatment in Ar/H_2, followed by thermal annealing in air (Figure 1i–

k). In another case, when pure cobalt acetate hydroxide prisms were used as precursors, the whole template could be consumed and converted into ZIF-67 hollow prisms due to the inside-out diffusion of Co^{2+} ions. Then crystalline hierarchical CoS_2 prisms with multistage hollow interiors were obtained by a subsequent sulfidation reaction and heat treatment in a nitrogen atmosphere (Figure 1l–n).[97] In this assembly strategy, whether a solid material can be used for MOF synthesis is determined by its lattice enthalpy.[103] In addition, the amount of organic ingredients and the choice of solvent play significant roles on the structural feature and stability of hollow structures.

Liquid–liquid interfacial reaction-induced assembly involves droplets or emulsions containing metal ions that are used as precursors and templates for the synthesis of hollow MOF capsules in another immiscible solvent containing organic ligands.[104-107] The coordination reaction between the metal nodes and the organic ligands in this case was localized at the interface of these two immiscible liquids for the formation of a MOF layer. For example, Ameloot and co-workers developed the fabrication of hollow HKUST-1 capsules by introducing copper acetate aqueous solution as droplets into 1-octanol (ligand solution) with microfluidic equipment as illustrated in **Figure 2**a–f.[106] When the two immiscible solutions are mixed evenly, the coordination reaction between the Cu nodes in aqueous droplets and the surrounding BTC ligands occurs only at the liquid–liquid interface, leading to the formation of hollow spherical $[Cu_3(BTC)_2]$ capsules that well inherit the droplet shape. The key to this strategy is the usage of two immiscible solutions; therefore, it is suitable for the fabrication of various other MOFs such as MIL-88A by simply changing the corresponding precursor solutions.[105] The diameter of the resulting hollow capsules can be changed by a small extent by adjusting the flow rates of the precursor solutions and the

capillary diameters (Figure 2g–m). The thickness of the shell was strongly influenced by the range of the interfacial layer between two immiscible solvents. For instance, by adding ethanol to the aqueous templating droplets, the liquid–liquid interface is made less confined in a narrow range as the ethanol diffuses out, resulting in the formation of a thicker macroporous MOF shell as shown in Figure 2f. The thickness of the shell is also proportional to the concentration of precursors.[107] Double-shell hollow capsules were successfully fabricated by serially coupling two pieces of microfluidic T-junctions (Figure 2m). Moreover, various kinds of functional substances ranging from inorganic nanoparticles to bioactive enzymes can be wrapped in the hollow capsules by directly dispersing them into the precursor solution.

In addition, metallo-surfactant-templated miniemulsion droplets were reported as templates and precursors for the fabrication of mesoporous metal coordination polymer (Prussian blue (PB) and its analogues (PBAs), hexacyanometalates, coordination networks with cyano ligands like MOF analogues) nanoshells with tunable size by a coordination polymerization reaction at the outer ring of the droplets.[108-110] For example, by mixing an organometallic surfactant (poly(ethylene glycol)-*b*-poly(propylene glycol)-*b*-poly(ethylene glycol) terminated with pentacyano(4-(dimethylamino)pyridine)ferrate (EPE-Fe)) with water, toluene and hexadecane in a certain proportion, miniemulsion droplets with a pentacyanoferrate periphery can be formed. The miniemulsion periphery polymerization is initiated by metal ions (e.g., Fe^{3+}, Gd^{3+}, or Er^{3+}) through a coordination reaction with pentacyanoferrates of the miniemulsion droplets. Subsequently, the surfactant core parts are removed via metal-assisted ester hydrolysis, resulting in hollow mesoporous PB/PBA crystal structures. It should be noted that the above synthesis-based emulsion templates all involve two immiscible solvents

containing two reactants, respectively. Interestingly, there is another special emulsion-template-induced synthesis of hollow MOFs by the spray-drying technique, which requires only a solvent to dissolve the reactants.[111, 112] By using a two-fluid nozzle, the solution of the precursors is first atomized into a spray of microdroplets. Then, each precursor droplet is suspended by a gas stream and heated to a certain temperature, which causes the solvent to begin evaporating and induces the precursors to diffuse radially to the droplet surface. When the critical concentration for reaction is reached at the surface, the nanoMOFs begin crystallizing at the surface and gradually form a well-packed shell. The spray-drying induced interfacial assembly provides a versatile methodology to construct multicomponent MOF superstructures.

2.1.2. Stepped Dissolution–Regrowth

In spite of the advantage of easily tuning the morphology and composition, some drawbacks of the template-mediated assembly strategy should be overcome, especially for hard-template synthesis. For example, its synthetic process is complex and high-cost, and requires post-synthesis removal of the templates, which is time consuming and hinders large-scale production. By comparison, the template-free and stepped dissolution–regrowth approach provides a promising and economical method to generate hollow MOF architectures. In recent years, such stepped dissolution–regrowth processes based on different reaction types have been widely reported for the formation of hollow MOF nanostructures, including the inside-out Ostwald ripening process and metastable core-directed secondary growth. Without an external template, this strategy simplifies the synthesis and reduces the cost.[113]

Ostwald ripening has been proven to be an effective template-free strategy that is widely used in the fabrication of hollow structures of diverse functional materials.[114-117] According to the IUPAC definition, Ostwald ripening refers to the phenomenon of "dissolution of small crystals or sol particles and the re-deposition of the dissolved species on the surfaces of larger crystals or sol particles".[118] The coarsening and recrystallization process occurs because smaller crystal or sol particles possess a higher surface energy; hence, their total Gibbs energy is greater than that of larger ones, giving rise to an apparent higher solubility. The formation process of hollow structures via the Ostwald ripening mechanism is induced by mass diffusion from the interior of smaller solid aggregates to the exterior, larger crystallites. For the synthesis of hollow MOFs, in the initial stage, a large amount of the small coordination polymer nucleus crystallizes out from the precursor solution due to the high concentration of metal ions and polymer ligands and quickly aggregates into larger, solid spherical particles to reduce the surface energy. With the decrease in reactant concentration to below the critical nucleation level, no further nucleation occurs, and the outer crystallites of the aggregates continue to grow into larger crystal particles at a lower growth rate. As the reaction proceeds, a hollow interior is generated by dissolution and diffusion out of the internal smaller and less compact solid aggregates and regrowth onto the external larger crystallites to reduce the high Gibbs energy of the overall system. As an example, Hou et al. demonstrated the synthesis of hollow ferrocenyl coordination polymer microspheres with microporous shells using the Ostwald ripening strategy, as depicted in **Figure 3**a.[62]

For the metastable core-directed secondary growth, it is proposed that the initially formed MOF solid lump should be an unstable and kinetic product, which is induced by strong coordination interactions between the metal nodes and polymer ligands in the supersaturated

precursor solution. Then, under thermodynamic conditions, these initially formed metastable and kinetic products will further interact with the remaining reactants in the solution and act as precursors and templates for the secondary growth of another kind of MOF material. Compared with the initially formed solid MOF, the final crystalline hollow MOF usually has different compositions or structures that are thermodynamically more stable under the experimental conditions.[64, 66, 113, 119-121] During this process, the growth of hollow MOFs can be divided into three stages: (1) the formation of solid MOF particles at the beginning of the reaction, (2) the gradually dissolution of the initially formed solid MOF while a new MOF simultaneously begins to grow on the surface of the initial MOF, and (3) the final formation of hollow structures. For instance, Oh et al. demonstrated the fabrication of hollow MOF microspheres through a one-pot solvothermal reaction of $Zn(NO_3)_2$ and trimesic acid (H_3BTC). The initially formed solid Zn-BTC microspheres were quite similar to the final hollow Zn-BTC in composition but different in crystallinity and porosity, as depicted in Figure 3b.[64] The poorly crystalline and nonporous solid Zn-BTC spherical products were quickly formed at the beginning of the reaction. Then, under a solvothermal condition, the initial solid Zn-BTC spherical particles gradually dissolved and regrew into more stable, highly crystalline, and porous hollow Zn-BTC microparticles. In another case, Wang et al. reported the synthesis of hierarchical Zn/Ni-MOF-based nanocages with heterometallic MOF systems.[66] The originally formed nanocubes possessed the MOF-5 crystal structure with a higher proportion of Zn^{2+}. Under the solvothermal condition, the remaining Ni^{2+} will partially replace Zn^{2+} and induce the transformation of the crystal structure from Zn/Ni-MOF-5 to thermodynamically favored Zn/Ni-MOF-2 with the gradual formation of hollow nanocages. It is worth mentioning that the coordination flexibility of the structural transformation in the

heterometallic MOF systems induced by the polymeric architectures can be expanded to other bimetal or mixed-ligand systems.[65, 119-122]

2.1.3. Selective Chemical Etching

Chemical etching is another widely utilized strategy for the synthesis of hollow nanostructures and is based on the inhomogeneous nature in solubility and chemical stability between the internal and external regions of the MOF crystals.[123] For most MOFs, the weak stability of the metal–ligand coordination bond is a crucial factor for etching technology, and the structure can be decomposed by accelerated hydrolysis of the coordination bonds in acidic or alkaline solutions.[124] Differences in the strength (related to defects or crystallinity) and shielding of coordination bonds are important factors causing inhomogeneity in MOF crystals. In recent years, various hollow MOF architectures have been fabricated by etching away their inner part of their corresponding templates based on the structural inhomogeneity of MOF crystals or a surface-protection process.

The structural inhomogeneity of the MOF crystals generally originates from the density of metal–ligand bonds along different crystallographic orientations[70] and the uneven distribution of defects.[71, 125, 126] The anisotropy of the crystal structure leads to different chemical compositions of exposed vertices, edges, and crystal facets. The crystallographic surface featuring a high density of coordination bonds will be preferentially etched. For instance, Avci et al. reported the formation of ZIF-8 and ZIF-67 microcages with four opening holes in the shells through a uniform and controlled solution-based anisotropic etching process of ZIF crystals.[70] In ZIF crystals, there exist several Zn-2-methylimidazole

coordination bonds in the {100} and {211} planes, while none of these bonds are present in the {110} and {111} planes, as shown in **Figure 4**a. For rhombic-dodecahedron-shaped ZIF crystals with only the twelve {110} facets exposed, the etching process is preferentially initiated from the four equivalent threefold vertices of the 12 {211} edges in acidic (xylenol orange) XO/HCl solution (pH 2.5). The morphological evolution of selectively etched ZIF crystals is illustrated in Figure 4b–h.

Defects in MOF crystals, such as incompletely coordinated metal nodes and grain boundaries, can significantly reduce the chemical stability. The inner region of MOF crystals prepared using solution-based methods is usually more defective due to the surface-energy-driven crystallization process, which enables the etching reaction to preferentially begin from the internal regions. Recently, by application of this feature, Hou et al. demonstrated the construction of multishelled single-crystalline hollow chromium (III) terephthalate MOFs (MIL-101) through an alternating crystal growth and etching process, as shown in Figure 4i–q.[71] Interestingly, the cavity size and shell thickness could be tailored by tuning the MOF nucleation and crystallization processes. The anisotropic distribution of defects can result in a nanostructure with complex interior voids through the chemical etching process, which is good for enhancing its physical and chemical properties. For example, in the case of Ni–Co PBA nanocubes fabricated via a typical co-precipitation reaction, defects of concentration in corner and edge areas are high due to the large curvature and high surface energy there. Thus, the etching rate along the diagonals of the nanocubes is faster, leading to the formation of these novel nanocages of Ni–Co–PBA consisting of pyramidal walls (Figure 4r–z).[125] Similarly, Co–PBA nanoboxes are obtained by etching the cube-shaped crystals of Co–PBA with ammonia.[126]

Using the structural inhomogeneity to etching is a facile method; however, for most MOF crystals, their structures and compositions are homogenous. Another feasible method is the surface protection induced etching, which involves shielding the coordination bonds on the surface of MOF crystals with a layer of stabilizing agents to prevent the corrosion of the surface. The representative stabilizing agents mainly include PVP,[72, 127] phenolic acids (i.e., tannic acid (TA) or gallic acid (GA)),[69, 128, 129] poly(vinylphosphonic acid) (PVPA),[130] and so on. In the case of PVP-protected etching, the PVP molecules tend to adsorb on the surface of MOFs through a weak coordination interaction with metal nodes. The adsorption of PVP will cover the coordination bonds and partially block the surface channels, thus shielding the coordination bonds from etchants; as a result, the etching rate in the surface slows down, and a hollow cavity is generated in the core part of the MOFs. As an example, Hu et al. demonstrated the fabrication of hollow-structured PB mesocrystals via HCl etching under the surface protection of PVP.[72] PB crystals are typical porous coordination compounds consisting of mixed-valence iron(III) ions coordinated by CN bridges. The H^+ ions can be diffused into the core of the PB mesocrystals through small pores (or defects) between directionally aggregated PB nanocrystals. In the presence of an appropriate amount of PVP, the etching speed in the core was relatively fast due the higher concentration of H^+ ions, generating the interior hollow cavity. In contrast, without the addition of PVP, the distribution of H^+ ions in the PB mesocrystals was relatively uniform, and the etching reaction occurred in the whole mesocrystal region, resulting in the random generation of macro/mesoporous structures. It is worth noting that too much PVP will totally cover the surface of PB nanocubes, and H^+ ions will be completely shielded outside, which will result in no significant changes in the structure of the PB precursors after the etching process. Therefore, it is crucial to control the ratios of stabilizing agents and MOF precursors.

Unlike PVP, the TA, GA, and PVPA can simultaneously act as surface-modification and etching agents for MOFs (**Figure 5**a,b).[69, 128, 129] Taking TA as an example, on the one hand, TA molecules can uniformly adsorb on the MOFs surface due to their strong chelation ability with metal nodes[131, 132] and the adsorbed TA molecules act as a tutelar agent by covering the coordination bonds and partially blocking the MOF channels. On the other hand, the protons released from the weakly acidic TA agents can break the coordination bonds in the framework of MOFs mildly. More interestingly, the TA molecules adsorbed on the surface of MOFs can modify the surfaces, transforming them from hydrophobic to hydrophilic, which promotes the diffusion of protons into the interior of the MOFs. Therefore, the etching reaction can be confined to the inside MOFs. GA and PVPA are slightly different from TA. The adsorption of GA on the surface of MOF is not uniform; as a result, the shell of the hollow crystals etched by GA contains "nanoflakes" (Figure 5e). In the case of PVPA, due to the strong binding effect between phosphonates and Zn(II), the MOF nanocrystals will be broken into separate parts and dragged into the defining shell regions after the adsorption of PVPA, forming a layer of a PVPA/MOF composite shell resistant to etching from the H^+ ion (Figure 5n–t).[130] In this way, the shell thickness of the hollow structure is proportional to the amount of PVPA etching agent.

2.2. Controllable Conversion of Solid MOFs with Predesigned Composition and Morphology into Hollow Structures

Compared to the previous category, directly converting solid MOFs into hollow-structured materials significantly simplifies the synthesis process, which provides a promising and

economical way to synthesize hollow-structured materials. This strategy usually involves optimized solution-based reactions or controlled pyrolysis processes. Due to differences in the chemical and thermal stability of MOF precursors, the conversion mechanisms from MOFs to hollow materials vary depending on the precursors. The conversion conditions, such as annealing temperature and time, gas atmosphere, and/or the reactants and solvents used, also need to change accordingly. The internal mass/volume loss is believed to be the key process during the transformation reaction. According to the reaction processes, the synthetic strategies can be categorized into three parts: interfacial ion exchange, heterogeneous contraction, and self-catalyst pyrolysis.

2.2.1. Interfacial Ion Exchange

Solid MOF precursors can react with suitable chemicals in solution to form a rigid shell at the solid–liquid interface with simultaneous transformation or etching of the inner core into void space. This strategy is widely utilized in the transformation of solid MOFs toward diverse hollow functional materials. For example, the chemical transformation of MOF precursors via an exchange reaction of anionic ligands with various reactants (anionic ions) in solution is a general phenomenon for most MOFs, suggesting that the chemical bond between the metal cluster and ligand linkers is reversible.[134-139] Since ion-exchange reactions are actually solid–liquid interface reactions, the composition of the reactants in the liquid phase will determine the types of ion-exchange reactions. According to the types of reactants, interfacial ion-exchange reactions are divided into single-anionic-ion-exchange reactions and exchange reactions involving multiple ions.

For the single-anionic-ion-exchange reaction, it is very simple; that is, only one anion in the liquid phase participates in the interfacial reaction. Typically, Zhang et al. demonstrated the synthesis of complex hollow microboxes via the ion-exchange reaction of the PB template with different alkaline substances in solution (**Figure 6**a–f).[140] To be more specific, the OH^- ions in alkaline solution will replace $Fe(CN)_6^{4-}$ to deposit a layer of iron hydroxide shell near the surface area of the PB. As the reaction progresses, OH^- ions diffuse inward to the porous $Fe(OH)_3$ shell and continue to react with the outward diffusion of Fe^{3+} ions producing $Fe(OH)_3$ clusters on the preformed $Fe(OH)_3$ shell (Figure 6a,b). The whole PB microcube is gradually depleted, accompanied by the growth of the $Fe(OH)_3$ shell, and the non-equilibrium interdiffusion process of Fe^{3+} and OH^- ions through the porous $Fe(OH)_3$ shell leads to the formation of well-defined $Fe(OH)_3$ microboxes with a large hollow interior. In addition to the single-shelled structure, yolk–shelled or multishelled structures can be achieved by controlling the reaction kinetics using a concentrated alkaline solution at an elevated temperature (Figure 5e,f). Apart from OH^- ions, a similar post-synthetic ion exchange can occur between MOFs and other anions, such as S^{2-} ions,[141-147] VO_4^{3-} ions,[148, 149] VO_3^- ions,[150] Se^{2-} ions, [151] and so on, released from their corresponding compounds toward the preparation of metal sulfides, metal vanadium oxides, and metal selenide, respectively. Figure 6g–i shows a typical example of well-defined hollow amorphous $Co_3V_2O_8$ nanocubes fabricated via an ion-exchange reaction of ZIF-67 with different VOT (VO^{3-}) concentrations.[148] Another typical example shows the time-dependent ion-exchange reaction between bimetallic ZIF crystals and S^{2-} for the synthesis of hollow bimetallic sulfide polyhedra (Figure 6j–m).[141] At the beginning of the sulfidation procedure, S^{2-} ions quickly react with metal ions on the MOF surface to form a thin layer of sulfides, which then acts as a

physical barrier between the outside sulfide ions and the inner metal ions. Due to the ionic radius of metal ions (72–74 pm) being significantly smaller than that of S^{2-} ions (184 pm), the outward diffusion of metal ions is much easier than the inward diffusion of S^{2-} ions. Therefore, the inner organic framework is gradually dissolved, and the released metal ions penetrate the preformed shell to react with S^{2-} ions on the outer surface, which finally produces a hollow void inside the shell. Moreover, by the S^{2-} ion-exchange reactions, core–shell ZIF crystals (ZIF-67@ZIF-8/ZIF-67) and Ni–Co–Fe PBA nanocubes are also converted into hollow-structured sulfides.[138, 152]

The single-anionic-ion exchange reaction usually results in a relative single component of the shell. Actually, by varying the reactants in the liquid phase, it is possible to construct complex shells with multiple components.[153-158] Lyu et al. demonstrated the conversion of Co-MOF into a hollow-structured $CoMoO_4$–$Co(OH)_2$ hybrid by using Na_2MoO_4 as a reactant, as shown in **Figure 7**a–d.[154] The presence of Na_2MoO_4 can provide not only MoO_4^{2-} to the formation of $CoMoO_4$, but also an alkaline environment for the formation of $Co(OH)_2$ around the ZIF-67 cores. On the other hand, ZIF-67 crystals will be slowly etched through hydrolysis in the presence of water, yielding 2-methylimidazole (2-MIM) linkers and Co^{2+} ions. The well-matched ion exchange and etching step in the interfacial reaction result in the nanocage structure that well inherits the morphology and dimensions of the MOF precursor. With the formation of a shell, the inward diffusion of MoO_4^{2-} and OH^- anions becomes slower and the outward diffusion of Co^{2+} becomes faster, which leads to the formation of void space within the $CoMoO_4$–$Co(OH)_2$ shells. Except Na_2MoO_4, similar alkaline precursors such as K_2SnO_3, $NaAlO_2$, $NaBO_2$, Na_2SiO_3, and Na_2SiO_3 are also used in the ion-exchange reaction of PB and produce hybrid MO_x–$Fe(OH)_3$ microboxes (Figure 6c).

In addition, the reactants in the liquid phase can be extended to other metal salts to cause different interfacial reactions. For example, nickel nitrate was used to react with ZIF-67 to form NiCo-LDH hollow polyhedral nanocages through a hydrolysis-controlled ion-exchange and etching dual process.[157, 159, 160] In this case, the hydrolysis of metal ions will generate protons to decompose the ZIF-67 and at the same time, Ni ions and hydroxyl will co-precipitate with released Co^{3+} ions (Co^{2+} will be oxidized in the presence of NO^{3-}) to form bimetal LDH on the surface of MOF precursor. Specially, a prethermal treatment of ZIF-67 crystals under N_2 at 400 °C for 2 h can lead to the formation of an amorphous carbon/LDH hybrid hollow nanostructure with enhanced conductivity (Figure 7e–k).[156] As a more complicated example, Yu et al. demonstrated the synthesis of Ni–Co–MoS_2 nanoboxes by reacting ammonium thiomolybdate with Ni–Co PBA nanocubes.[153] NH_3 decomposed from ammonium tetrathiomolybdate will dissolve the Ni–Co PBA by exchanging cobalt cyanide and complexing with Ni(II). At the same time, MoS_2 nanosheets produced from the ammonium tetrathiomolybdate start to grow on the surface of the nanocubes under solvothermal conditions, and some uncoordinated nickel and cobalt ions will be spontaneously doped into MoS_2 nanosheets to form Ni–Co–MoS_2 nanoboxes. In summary, complex hollow-structured materials with various components can be prepared from solid MOF precursors by manipulating the interfacial ion-exchange reactions.

2.2.2. Heterogeneous Contraction

Heterogeneous contraction induced by the non-equilibrium heat treatment is a simple and convenient strategy widely used in the fabrication of hollow micro/nanospheres with controllable

interior structures.[161, 162] This strategy is based on the gradual decomposition of MOF precursors from the outside to the inside, induced by a temperature gradient. The hollow interior is formed due to the separation of the dense shell and the inner core generated in situ during the annealing process. In most cases, the thermal degradation of MOFs under a high temperature is a result of cleavage of the coordination bond, followed by linker carbonization or combustion. However, reasonable control of the thermal-treatment conditions can enable the formation of the hollow structures via a heterogeneous contraction process. Several parameters play crucial roles in this process. First, only a relatively high heating rate (R) can induce the initial formation of a layer of dense, rigid shell, due to the large temperature gradient (ΔT) generated along the radial direction. Thereafter, it is conceivable that two forces exist in opposing directions, simultaneously acting on the interface between the inner core and the rigid shell (i.e., heterogeneous contraction occurs). One is the contraction force (F_c) induced by the inward shrinkage of the core, resulting from volume loss during the decomposition or combustion of organic ligands. The other is the adhesion force (F_a) from the relatively rigid shell related to the coordination bond strength and number of linkers connected to each node, which resists the inward contraction of the inner core. Obviously, reducing the adhesion force and increasing the contraction force is beneficial for separation of the inner core from the shell. It can be seen that the crucial step in the heterogeneous contraction strategy is the formation of a layer of dense rigid shell. Under high R, some MOFs like amorphous or low-crystalline with optimized composition may rapidly produce a layer of shell in situ,[163-166] however, for highly crystalline and homogeneous MOF crystals, they are difficult to first produce shell using this method. For such MOFs, an alternative and effective strategy is coating the MOFs with a layer of rigid shell to prevent structure collapse and induce outward contraction. Therefore,

the heterogeneous contraction strategy can be divided into contraction induced by both the shell generated in situ and the external rigid shell.

Contraction induced by the shell generated in situ provides a relatively simple means to obtain complex hollow structures by controlling the temperature gradient. Typically, Wu et al. demonstrated the fabrication of $Ni_xCo_{3-x}O_4$ multishelled hollow microspheres (MS-HMSs) with low-crystalline Ni–Co–BTC solid microspheres as precursors, as shown in **Figure 8**a–h.[167] A high R will produce a large ΔT along the radial direction, inducing the formation of a layer of a $Ni_xCo_{3-x}O_4$ shell on the surface of Ni–Co–BTC spheres. As the calcination continues, the volume loss caused by the oxygenolysis of the organic ligands will promote the inward shrinkage of the Ni–Co–BTC core. Due to the weak F_a in this kind of amorphous material, the core is detached from the preformed shell, resulting in a yolk–shelled intermediate. Then, the as-generated inner core will repeat the above formation process of a solid or hollow structure two or three times, depending on the remaining ΔT in its radial direction. Lastly, due to degradation of the ΔT, F_a is strong enough to cause the outward contraction of the inner core, leaving a void at the center. Finally, solid Ni–Co–BTC transforms into the unique structure of a multishelled hollow microsphere.

The thermodynamic properties of the MOF composition play crucial roles in rapidly producing a layer of shell in situ under high R. Rational optimization of the MOF composition by introducing guest organic molecules/metal particles has been demonstrated to be an effective means to control the pyrolysis process of MOFs.[170, 171] For example, Zhan et al. proposed a simple and novel approach for the synthesis of hybrid CuO/ZnO multishelled hollow architectures by copper-assisted oxidative degradation of amorphous ZIF-90 (a_mZIF-

90), as illustrated in Figure 8i–o.[168] The as-prepared a$_m$ZIF-90 sub-micrometer spheres loaded with Cu nanoparticles can be converted into hollow multishelled composites by rapid thermal treatment in air. In contrast, for pure a$_m$ZIF-90 or a$_m$ZIF-90 loaded with Au particles, the same heat treatment produces only solid products. It is believed that the preloaded Cu nanoparticles can accelerate the thermal oxidative decomposition of organic species a$_m$ZIF-90 via a catalytic effect. Cu-accelerated oxidative pyrolysis of a$_m$ZIF-90 induces the rapid formation of a layer of CuO/ZnO shell, and then the core detaches from the shell due to a strong F_c against F_a. Similar to the Ni–Co–BTC MOF, this process repeats two or three times and produces multishelled structures. Interestingly, when the Cu-loaded a$_m$ZIF-90 sample was calcined under a non-oxidizing gas (Ar) ambiance, only solid products were achieved, even at a relatively high temperature (400 °C), which further confirms the oxidative pyrolysis process of a$_m$ZIF-90. Such a phenomenon was also observed in the Ni-MOF sphere (Ni–BTC) by introducing copper ions through a cation-exchange process (Figure 8p–t).[169] The introduction of Cu ions or nanoparticles leads to rapid generation of the shell in situ by catalyst-accelerated oxidative pyrolysis, suggesting the importance of composition in the heterogeneous contraction process.

Although various hollow structures have been achieved by contraction processes induced by the shell generated in situ, this strategy depends on the crystallinity and composition of the MOFs. However, the external-rigid-shell-induced contraction provides a more flexible strategy to convert more types of MOFs to hollow structures.[172, 173] For example, Liu et al. reported the construction of hollow mesoporous carbon nanocages (HMCNCs) via thermal decomposition of a layer of mesoporous SiO_2-coated ZIF-8 nanocubes. During pyrolysis, the ZIF-8@mSiO_2 precursors started to inwardly decompose from the outermost ZIF-8 crystals

embedded in the SiO_2 shell because of the temperature gradient along the radial direction of the nanocomposites (Figure 9).[174] Then, the strong connection between the rigid, thick silica coating and the ZIF-8 crystals provided an outward driving force to pull the carbon produced by the consequent decomposition to adhere on the silicon surface and prevented the collapse or shrinkage of the structure. The intrinsic mass loss (release of gases, e.g., NH_3 and $(CN)_2$) of carbonized ZIF-8 led to the generation of voids and mesopores. After etching away the silica shell, a hollow carbon nanocage with a multilevel porous shell is produced. In contrast, when a sufficiently nonrigid thin silica coating is used, the overall carbonization is inward, resulting in the formation of a nonhollow mesoporous carbon architecture.

Except for porous silica, various other materials can also be used as a rigid shell of MOFs, such as polymers[175-179] and other kinds of MOFs.[180-184] These materials decompose to form shells prior to MOFs and sometimes these shells combine with the pyrolysis products of MOFs to form composite hollow materials. For instance, Liu et al. reported the synthesis of double-shelled NC@Co-NGC nanocages via a rigid-shell-induced outward contraction using core–shell-structured ZIF-8@ZIF-67 dual MOFs as precursors, as shown in **Figure 10**.[185] The difference in thermal stability between ZIF-8 and ZIF-67 is the key factor. In detail, under the calcination, the less stable ZIF-67 would decompose first to form a rigid shell of CoO/carbon around ZIF-8 cores at above 500 °C. On the other hand, due to the same topological structure, ZIF-8 and ZIF-67 will form a close combination at the interface, perhaps caused by interdiffusion of the two MOFs. Thus the rigid CoO/carbon composite shells would provide an outward pulling force at the interface between them and the ZIF-8 cores. In the following calcination process, the decomposition of core–shell-structured ZIF-8@CoO/carbon undergoes a rigid-shell-induced outward contraction similar to that described

above. The porous outer shell of NC@Co-NGC nanocages comes from the catalytic carbonization of ZIF-67, while the inner dense shell is derived from the adhesion of high-temperature-carbonized ZIF-8. As a comparison, when core–shell ZIF-67@ZIF-8 crystal particles are constructed and calcinated under identical conditions, only solid Co-NGC@NC nanoparticles, rather than hollow architectures, are obtained, which further confirms the mechanism of rigid-shell-induced contraction.

2.2.3. Self-Catalytic Pyrolysis

One emerging hot topic is the controllable conversion of precursor MOFs or their composites into carbon nanotubes (CNTs) or graphene tubes (GTs) with hollow structures by in situ self-catalytic pyrolysis reactions in which the MOF crystals or guest molecules provide both the metal catalysts and carbon sources.[186-188] Compared to the conventional chemical vapor deposition (CVD) processes, preparation of CNTs or GTs using MOFs as a precursor has broad application prospects due to the advantages of easy synthesis, relatively low temperature, environmental friendliness, and high yield. Moreover, the carbon structure and heteroatom component can be easily tuned by varying the type of MOFs and calcination conditions, such as pyrolysis temperature, reaction time, and gas atmosphere. For example, nitrogen-doped carbon nanotubes (N-CNTs) can be achieved by application of nitrogen-containing MOF precursors or encapsulating hetero-molecules (such as dicyandiamide) within. The introduction of appropriate amounts of hetero-molecules can effectively tune the N content, N-doped state, formation temperature, and morphology of the NCNTs.[189, 190] Obviously, the self-catalytic pyrolysis reactions depend strongly on the components of MOFs

or their composites. According to the type of MOF-based precursors, the self-catalytic pyrolysis reactions are divided into self-catalysis induced by a single MOF and self-catalysis induced by guest molecules.

Self-catalysis induced by a single MOF has been successfully applied in the synthesis of CNT-assembled hollow structures. The selected MOF crystals act as single precursors for both the nanocatalysts and carbon sources. In this process, the formation of highly active small metal nanocatalysts is the key step, as it controls not only the subsequent CNT growth but also the assembly morphology of the final product. As an example, Meng et al. reported a simple, general, and high-yield approach for the conversion of MOF crystals into N-CNT-assembled hollow structures using a controlled low-temperature pyrolysis method (Figure 10b–d).[191] In detail, the Co ions within the near surface region of the MOFs are first converted into uniformly distributed Co nanoparticles by reductive gases (CO, NH_3, and H_2) released from the pyrolysis of organic ligands. The holding temperatures are kept near the decomposition temperatures of selected MOFs in order to obtain a slow pyrolysis rate and prevent aggregation of the formed small Co nanoparticles into large particles. Second, due to the strong catalytic activity of Co nanoparticles, the organic residuals on the nanocatalysts are catalyzed into N-CNTs in a controllable way at a low temperature. Due to the preferential formation of highly active metal nanoparticles in the near surface regions, the subsequent catalytic growth direction of N-CNTs is from inside to outside, resulting in the generation of an interior cavity. A sufficient maintaining time is essential for the complete conversion of the MOF precursors because of the slow growth kinetics of the CNTs. As a comparison, high-temperature treatment (above the decomposition temperatures of MOFs) only results in carbon-coated large-metal-core nanoparticles. The low catalytic activity of the large metal

cores cannot enable the transfer of the surrounding carbon shells into the CNTs, suggesting the importance of the formation of highly active small metal nanocatalysts by controlling the temperature. Recently, Zhou et al. demonstrated the growth of small-diameter Co- and N-co-doped carbon nanotubes (Co/N-CNTs) by coating a layer of mesoporous silica ($mSiO_2$) on ZIF-67 to prevent the aggregation of Co nanoparticles.[192] Interestingly, the small Co nanoparticles can be maintained even at relatively high temperatures due to the protection of the $mSiO_2$ layer, which significantly improves the stability of the nanocatalysts compared to that without protection. Moreover, the $mSiO_2$ layer serves as a unique "sieve" to provide a novel external passageway for the outward growth of CNTs. This strategy provides a new means for efficient conversion of MOFs to small-diameter doped carbon nanotubes in inert atmospheres at high temperatures.

The abovementioned syntheses are carried out in an inert atmosphere, in which the treatment temperature has a great influence on the product. However, another study suggested that changing the gas atmosphere makes the synthesis more flexible. Lou et al. demonstrated the conversion of ZIF-67 to N-CNTs with hollow frameworks in a wide temperature range (600 °C to 900 °C) by introducing H_2 into the gas atmosphere (Figure 11e–j).[193] Because of the high reductivity of H_2, highly active small metallic Co nanoparticles are quickly formed through large-scale and rapid generation of crystal nuclei. Subsequently, a similar inside-to-outside growth of N-CNTs occurs, leading to generation of the hierarchical hollow architecture. Surprisingly, even at 900 °C, hollow N-CNT frameworks can be obtained in the presence of H_2. A high temperature can allow the complete pyrolysis of the template and increase the growth efficiency of nanotubes, leading to the growth of longer CNTs with a higher density and a much rougher surface, while a lower temperature results in numerous

short CNT clusters. Compared to the synthesis in an inert atmosphere, the presence of H_2 enables the conversion of MOFs to CNTs over a wider temperature range.

In addition to using the metals and organic ligands contained in the MOF itself to grow CNTs, a variety of guest molecules can also be introduced into the pores of MOFs and act as special metal catalysts and carbon sources to convert MOF precursors into other carbon structures. For example, Li et al. demonstrated the application of MOFs encapsulating iron acetate and dicyandiamide (DCDA) molecules in giant polyhedral cages as precursors for the preparation of large-diameter bamboo-like nitrogen-doped graphene tubes (N-GTs) (Figure 11k–n).[190, 194] The successful formation of N-GTs is found to be dependent on the precursors and heating temperature. First, the unique pore structure of MOFs plays a key role in the uniform dispersion of the guest species. Second, during the high-temperature treatment process, the guest Fe species will interact with MOF parents, resulting in the formation of Fe/Fe_3C particles, which catalyze the growth of the bamboo-like N-GTs. Third, the decomposition of DCDA releases large amounts of carbon nitride gases (e.g., C_2N^{2+}, C_3N^{2+}, and C_3N^{3+}) that, together with the MOF parent, coalesce into graphitized carbon doped with nitrogen. The role of DCDA is indispensable in catalyzing the growth of the unique graphene-tube-like carbon structures. Finally, in this case, a sufficiently high heating temperature (900–1000 °C) is necessary for the growth of the N-GTs. Overall, the comprehensive effects of the MOF template, DCDA, and Fe species led to the in situ self-catalytic growth of highly graphitized N-doped carbon architectures under a high annealing temperature.

3. Applications in Energy Storage and Conversion

3.1. Lithium-Ion Batteries (LIBs) and Supercapacitors (SCs)

LIBs play an important role in electrochemical energy storage. In recent years, tremendous efforts have been made to design and construct electrode materials with novel structures to improve the properties of LIBs. Due to the various advantages of hollow-structured materials, such as low mass density, robust structure, high surface area, and fast intercalation of Li^+ ions, the preparation of hollow electrode material has long been a focus in material synthesis. As discussed above, the unique compositions and flexible structures of MOFs make them ideal precursor materials for the preparation of hollow architectures. To date, various novel MOF-derived hollow architectures have been developed and applied as LIB electrodes. For instance, Lu et al. reported the construction of complex Co_3O_4@$Co_3V_2O_8$ hollow structures by taking advantage of the unique reactivity of ZIF-67 with the vanadium oxytriisopropoxide and studied their electrochemical performance as anode materials for LIBs (**Figure 12**a–c).[148] Due to the integrated merits of the two active components and the complex structure, triple-shelled Co_3O_4@$Co_3V_2O_8$ microboxes exhibiting superior lithium-storage performance with excellent rate capability, cycling stability, and reversible capacity (Figure 13e–g) were fabricated, superior to those of many other reported non-MOF-derived Co/V-based oxides.[199, 200] The high specific surface area of the complex hollow structure provides more electroactive sites to achieve higher specific capacity, and the multishell structure and reduced particle size allow intimate contact between the active material and the electrolyte, resulting in high-speed lithium insertion/removal and mechanical stability. Moreover, the complex hollow structure of the Co_3O_4@$Co_3V_2O_8$ microboxes is well maintained after long

discharge–charge cycles (Figure 12d), suggesting the superior stability of the hollow structure during repeated lithium insertion/removal processes.

Supercapacitors are another kind of promising energy-storage device with an ultrafast energy-storage rate, high power density, and excellent cycle life. The structure of the supercapacitor is similar to that of a battery, with two electrodes separated by an ion-permeable membrane. In this regard, the structural features of hollow architectures, such as high specific surface area and porosity, greater number of accessible active sites, and easy electrolyte penetration, can also help a supercapacitor to obtain high specific capacitance and excellent rate performance. For example, Zhang et al. demonstrated the synthesis of well-defined single/double-shelled Zn–Co–S hollow composite structures through a sequential chemical etching and sulfurization strategy (Figure 12 h–k) and investigated these hollow structures as electrodes for supercapacitors. The high specific surface, weight fraction of active species, and suitable Zn/Co molar ratio of the double-shelled Zn–Co–S hollow composite structures resulted in improved performance, such as enhanced specific capacitance (as high as 1266 F g^{-1} at 1 A g^{-1}) and excellent rate capability as a battery-type electrode material for hybrid supercapacitors, as shown in Figure 12l, m. Interestingly, the double-shelled Zn–Co–S improved the cycling stability (91% maintained after over 10 000 cycles), while the single-shelled Zn–Co–S showed a capacitance loss of 19 % under the same conditions (Figure 12n). After a cycling test, the structure of the double-shelled Zn–Co–S is also well preserved, similar to those of the Co_3O_4@$Co_3V_2O_8$ electrode materials, further demonstrating the stability of MOF-derived structures. Overall, the electrochemical performance of double-shelled Zn–Co–S is significantly better than that of many reported zinc/cobalt-sulfide-based electrode materials for hybrid supercapacitors.[201]

3.2. Electrocatalysis for HER, OER, and ORR

Water splitting, metal–air batteries, and fuel cells are energy-conversion technologies that are of critical importance to address the future energy crisis and environmental issues. The hydrogen evolution reaction (HER) and oxygen evolution reaction (OER) are the two important half reactions of water splitting. Also, both the OER and oxygen reduction reaction (ORR) play important roles in metal–air batteries. The ORR is also considered to be one of the fundamental electrochemical reactions for fuel cells. Among all of the reported electrocatalyst systems, hollow architectures with an enhanced specific surface area, a greater number of assessable active sites per unit geometric area, a shortened mass/charge transfer distance, and a limited aggregation of nanosized subunits have been viewed as highly advantageous in electrocatalytic reactions. Noble-metal-based catalysts, e.g., Pt, RuO_2, and IrO_2, show remarkable activity but are limited due to their low abundance and high cost. Therefore, developing highly efficient and stable nonporous electrocatalysts is critical for practical application. MOF-derived hollow-structured materials possess greatly advantageous features in terms of tailorable composition and multilevel porosity, which makes them highly efficient as electrocatalysts.

Molybdenum carbide has been widely investigated as a high-performance HER electrocatalyst under both acidic and basic conditions in light of its Pt-like electronic structure, low cost, high abundance, and good electrical conductivity.[202, 203] Hollow molybdenum-carbide-based hybrid nanoparticles have been prepared through a simple MOF-assisted synthetic strategy as electrocatalysts for an efficient hydrogen-evolution reaction.[119]

Initially, the Mo-based polyoxometalate-incorporated Ni-MOF hollow structure is prepared through a dissolution–regrowth process. Then, carbon nitride polymer is coated on the surface of the hollow precursor. Such a unique precursor enables a confined and uniform carburization reaction without particle coalescence or detachment during the annealing process. As a consequence, the combination of compositional advantages (molybdenum carbide and Ni NPs) and unique architecture (i.e., hollow nature and carbon layer coating) make the product a highly efficient and stable HER catalyst. The as-prepared samples exhibited a small overpotential of 123 mV to obtain a current density of 10 mA cm^{-2}, a small Tafel slope of 83 $mV \cdot dec^{-1}$ in 1 M KOH solution, and excellent stability.

Transition-metal phosphides (TMPs) are another kind of widely studied highly efficient catalysts for an HER.[204] Similarly, further improvement of the catalytic performance of TMP-based catalysts could be achieved by constructing suitable hollow nanostructures with more exposed surfaces and active sites. For instance, Pan et al. demonstrated the fabrication of a hollow composite of CoP nanoparticles embedded in N-doped carbon nanotubes via a successive pyrolysis–oxidation–phosphidation process using core–shell ZIF-8@ZIF-67 as a precursor (**Figure 13**a).[183] Benefiting from the synergistic effects between highly active CoP nanoparticles and a N-doped carbon nanotube hollow polyhedron (NCNHP), the CoP/NCNHP hybrids exhibited remarkable catalytic activity for the HER, affording a current density of 10 $mA \cdot cm^{-2}$ at small overpotentials of 140 mV in 0.5 M H_2SO_4 (Figure 13c) and 115 mV in 1 M KOH, which is much better than that of the nonhollow CoP/NCP (Figure 13b) (234 and 148 mV, respectively). Moreover, the CoP/NCNHP catalyst exhibits small Tafel slopes of 53 and 66 $mV \cdot dec^{-1}$ in 0.5 M H_2SO_4 and 1 M KOH, respectively, verifying its favorable electrocatalytic kinetics for the HER. In addition to the HER, the as-prepared

hollow CoP/NCNHP nanocomposite exhibited excellent electrocatalytic properties for the OER. The assembled water-splitting cell with a hollow CoP/NCNHP nanocomposite as both the anode and cathode yields a potential as low as 1.64 V to achieve a current density of 10 $mA \cdot cm^{-2}$. In another case, Han et al. demonstrated the synthesis of porous Ni–Co mixed-oxide nanocages for the OER (Figure 13e) via a simple chemical etching of PBA cubes, followed by a low-temperature annealing treatment in air.[125] The Ni–Co mixed-oxide nanocages are constructed with six porous pyramidal walls, which provide the high specific surface area for adequate contact between the active sites and the electrolyte. As a result, the Ni–Co mixed-oxide cages exhibit excellent OER performances in an alkaline electrolyte, such as a small overpotential of 0.38 V at a current density of 10 mA cm^{-2} (Figure 13g), a small Tafel slope of 50 mV dec^{-1} (Figure 13h), and good durability that is obviously better than that of Ni–Co mixed-oxide porous cubes (Figure 13f), further confirming the advantages of hollow architectures with multilevel pore configurations.

Heteroatom-doped carbon materials have been intensively studied as potential electrocatalysts for the ORR. As described in Section 2.2.3, through control of the pyrolysis atmosphere, the ZIF-67 particles could be converted into hollow-structured N-doped carbon-nanotube frameworks (NCNTFs) (Figure 13i).[193] The as-prepared NCNTFs possess advantageous features—chemical composition, a hierarchical and robust shell of interconnected crystalline NCNTs, and an optimum graphitic degree and N-doping level—that are essential for high electrocatalytic activity and stability for the ORR and the OER. Remarkably, the NCNTF sample exhibits higher ORR activity than does the commercial Pt/C electrocatalyst in terms of half-wave potential ($E_{1/2}$; 0.87 V vs 0.84 V in Figure 13k). The NCNTF also outperforms most similar materials prepared using non-MOF-based

methodologies. In addition, The NCNTF catalyst shows negligible performance loss after a CV test, from 0.2 to 1.2 V for 5000 cycles (Figure 13l), suggesting the superior stability of the catalyst. The excellent stability of NCNTFs is ascribed to the robust framework structure composed of interconnected crystalline NCNTs, which retains its original morphology and structure after the cycling test, as confirmed by TEM analysis (Figure 13j).

Besides the abovementioned single-function catalysts, the development of low-cost bifunctional electrocatalysts with high activity is highly desired to reduce the complexity of renewable energy-storage and conversion systems. Metal–N-doped carbon hybrids (M–N–C) have shown exciting performance in the HER, OER, and ORR, with enhanced reaction kinetics and structural stability comparable to noble-metal catalysts. The controllable pyrolysis of MOFs represents one of the most efficient approaches for producing nanostructured M–N–C catalysts with uniformly distributed active sites. As a typical example, double-shelled composite carbon nanocages (Figure 13m) with N-doped microporous carbon (NC) as inner shells and Co–N-doped graphitic carbon (Co–NGC) as outer shells were prepared using the controlled thermal decomposition of core–shell ZIF-8@ZIF-67 crystals at a high temperature via a rigid-shell-induced contraction process.[185] The combination of highly active Co–NGC shells and a robust hollow NC structure with enhanced diffusion kinetics provides the double-shelled NC@Co–NGC nanocages with enhanced electrocatalytic activity and long-term stability as compared with Pt and RuO_2 catalysts toward the OER and ORR, respectively (Figure 13o). The overall oxygen-electrode activity is evaluated according to the difference in OER and ORR metrics ($\Delta E = E_{j=10} - E_{1/2}$). Remarkably, NC@Co–NGC exhibits a ΔE of 0.82 V, much lower than that of Pt/C (0.94 V),

RuO_2 (1.0 V), and especially solid Co–NGC (Figure 13n) (0.95 V), further revealing the positive effect of a hollow nanostructure on the electrocatalytic activity.

4. Conclusion and Outlook

Hollow-structured materials are promising candidates for many future technological applications due to various advantageous structural features: an enhanced surface-to-volume ratio, low density, a microreactor environment, higher loading capacities, and shortened transport lengths for both mass and charge. The distinct crystalline and porous structures and tailored compositions of MOFs make them outstanding precursors to create hollow-structured materials via various conversion reactions. Here, the recent advancements in the controlled construction of hollow-structured functional materials using MOFs as unique precursors are summarized, together with their promising applications in electrochemical energy storage and conversion. According to the features of MOF precursors, the synthetic strategies are broadly divided into two categories: the controllable synthesis of hollow MOFs and subsequent pyrolysis into functional materials and the controllable conversion of solid MOFs with predesigned composition and morphology into hollow structures. Based on the formation processes of hollow MOFs and the conversion processes of solid MOFs, the synthetic strategies are further conceptually grouped into six categories: template-mediated assembly, stepped dissolution–regrowth, selective chemical etching, ion exchange, heterogeneous construction, and self-catalytic pyrolysis. Each strategy contains at least two reaction types. By analyzing and discussing the fourteen types of reaction processes in detail, a systematic conversion mechanism from MOFs to hollow-structured materials is exhibited. It should be

noted that although the fourteen types of reaction processes are discussed separately, two or more reactions occur simultaneously in most cases. The combination and optimization of various conversion reactions will provide powerful capabilities for further design and synthesis of other novel hollow structures in a controllable manner.

Owing to the development of synthetic strategies and the understanding of reaction mechanisms, various MOFs have been converted into hollow-structured functional materials such as metal oxides, sulfides, carbon, and their composites. Such functional materials exhibit remarkable electrochemical performances due to their exceptional structures and compositions. As electrode materials for lithium-ion batteries, hybrid or multishelled metal oxides exhibit superior lithium-storage performances with excellent rate capability, cycling stability, and reversible capacity. The high specific surface area of the hollow structure provides more electroactive sites to achieve higher specific capacity, and the multishelled structure and reduced particle size allow intimate contact between the active material and the electrolyte. These exceptional structural merits also greatly help supercapacitors to obtain high specific capacitance and excellent rate performance. On the other hand, hollow architectures with an enhanced specific surface area, shortened mass/charge transfer distance, and limited aggregation of nanosized subunits are highly advantageous for electrocatalytic reactions due to the accessibility of a greater number of exposed active sites per unit geometric area. It is worth mentioning that some MOF-derived nonprecious hollow nanomaterials exhibited equivalent or even better electrocatalytic activity as compared with the noble-metal-based catalysts, which is vital for practical applications. These studies demonstrate that MOF-derived hollow-structured functional materials have superior properties for application in electrochemical energy storage and conversion.

Though great progress has been made in the preparation and application of MOF-derived hollow-structured materials, this research field is still in its infancy, and more effort is required to realize the practical usage of MOF-derived hollow structures. Several challenges and possible research directions for future work in this area are as follows.

(1) From a synthetic viewpoint, the precise control and manipulation of hollow structures with high complexity remain challenging. To improve the utilization efficiency of materials, it is highly desirable to controllably synthesize complex structures according to the needs of specific applications. Different applications place different demands on the structures. For example, in rechargeable batteries, electrode materials with hierarchical multishelled architectures and appropriate void ratios can deliver high volumetric energy densities and minimize side reactions associated with the exposed outer surface. In electrocatalysis, catalysts with 3D hierarchical porous architectures can maximize the accessible active surface to achieve high electrocatalytic activities. Therefore, exploring novel synthetic protocols for complex hollow structures based on the high flexibility of MOF superstructures is one of the most important research directions for the future.

(2) The controllable incorporation of different components such as heteroatoms (N, S, P, etc.) and metal-based species (carbides, nitrides, phosphides, etc.) is important for improving the properties of the resultant hollow-structured materials. In the multicomponent hybrids, each component plays a special role or possesses a unique function that can overcome the drawbacks of the individual counterparts and generate a synergistic effect for enhanced performance. Typically, MOF-derived hollow metal-oxide–carbon hybrids exhibit several appealing features, such as high electrical conductivity, short ion-diffusion paths, and excellent structural stability. To achieve multicomponent hybridization, MOF precursors will

be the best choice because their frameworks are designable and can be incorporated with various functional species of metal ions/clusters and organic linkers during the modular self-assembly process. Currently, the synthesis of hollow-structured materials is mostly limited to the ZIF or MIL series. In the future, MOFs with multiple metal centers and multiple ligand linkers need to be explored to precisely incorporate various components with controllable content and distribution.

(3) From the perspective of electrochemical applications, there is still a lack of in-depth understanding about the structure–property relationship of hollow-structured materials for electrochemical energy storage and conversion. The reaction mechanisms of various hollow-structured materials with lithium/sodium ions have not been thoroughly investigated. Similarly, little information is available about the real active sites and their corresponding catalytic mechanisms in MOF-derived ORR, OER, and HER catalysts. Furthermore, many studies simply attribute the enhanced electrochemical performance to the synergistic effect of the hollow structures and compositions; however, the real origin of such an effect has not yet been revealed. Future work should focus on comprehensive research of the relationship between the structure and the electrochemical characteristics. A combination of experimental and computational approaches should be used to discover the interior reaction mechanisms and reveal the effects of structural and compositional modification as well as their synergistic interactions.

(4) The use of MOF-derived hollow-structured materials is mainly limited to some simple electrochemical reactions. It is necessary to expand their applications to other reaction systems to offer new directions for the application of these new functional materials. Although intricate hollow structures have been extensively studied in LIBs, their applications

in sodium-ion batteries (SIBs), potassium-ion batteries (KIBs), Li–O_2 batteries, and Na–O_2 batteries have attracted little attention. For electrocatalysis, in addition to the ORR, OER, and HER, other emerging energy conversions, such as the CO_2 and N_2 reduction reaction, are essential for alleviating environmental and energy crises. The unlimited combinations of metal ions and organic ligands in MOF precursors will lead to a diverse range of possible hollow-structured materials. They will have different components and will exhibit different properties to meet the requirements of different applications.

In summary, the rapid development of hollow-structured materials from the controllable conversion of MOFs presents many new opportunities for batteries and catalysis. This novel approach provides a simpler and more designable way to achieve advanced electrode materials and electrocatalysts with desired structures and compositions, which will greatly promote the development of energy-storage and conversion technologies. Although MOF-derived hollow functional materials are still far from real industrial application, low-cost and industrial productions of MOFs have been proven to be feasible by improving the synthesis processes.[205, 206] With continued research in the related fields, a series of large-scale engineering and commercial applications will be developed in the near future.

Acknowledgments

Z.X.C. and Z.LW. contributed equally to this work. Z.X.C. and Z.LW. thank the Japan Society for Promotion of Science (JSPS) for providing the JSPS standard postdoctoral fellowship.

[1] J. Wang, Y. Cui, D. Wang, *Adv. Mater.* **2018**, 30, 1801993.

[2] Y. P. Zhu, T. Y. Ma, M. Jaroniec, S. Z. Qiao, *Angew. Chem. Int. Ed.* **2017**, 56, 1324.

[3] L. Yu, H. Hu, H. B. Wu, X. W. Lou, *Adv. Mater.* **2017**, 29, 1604563.

[4] H. C. Li, Y. J. Zhang, X. Hu, W. J. Liu, J. J. Chen, H. Q. Yu, *Adv. Energy Mater.* **2018**, 8, 1702734.

[5] S.-Q. Liu, H.-R. Wen, G. Ying, Y.-W. Zhu, X.-Z. Fu, R. Sun, C.-P. Wong, *Nano Energy* **2018**, 44, 7.

[6] J. Y. Jang, H. T. T. Duong, S. M. Lee, H. J. Kim, Y.-J. Ko, J. H. Jeong, D. S. Lee, T. Thambi, S. U. Son, *Chem. Commun.* **2018**, 54, 3652.

[7] K. Yang, Y. Liu, Y. Liu, Q. Zhang, C. Kong, C. Yi, Z. Zhou, Z. Wang, G. Zhang, Y. Zhang, N. M. Khashab, X. Chen, Z. Nie, *J. Am. Chem. Soc.* **2018**, 140, 4666.

[8] N. A. Dogan, E. Ozdemir, C. T. Yavuz, *ChemSusChem* **2017**, 10, 2130.

[9] J. Chun, S. Kang, N. Park, E. J. Park, X. Jin, K.-D. Kim, H. O. Seo, S. M. Lee, H. J. Kim, W. H. Kwon, Y.-K. Park, J. M. Kim, Y. D. Kim, S. U. Son, *J. Am. Chem. Soc.* **2014**, 136, 6786.

[10] W. Konicki, K. Cendrowski, X. Chen, E. Mijowska, *Chem. Eng. J.* **2013**, 228, 824.

[11] S. Shi, F. Zhang, H. Lin, Q. Wang, E. Shi, F. Qu, *Sens. Actuators B* **2018**, 262, 739.

[12] X. Li, D. Lu, C. Shao, G. Lu, X. Li, Y. Liu, *Sens. Actuators B* **2018**, 258, 436.

[13] X. W. Lou, L. A. Archer, Z. Yang, *Adv. Mater.* **2008**, 20, 3987.

[14] F. Caruso, R. A. Caruso, H. Mohwald, *Science* **1998**, 282, 1111.

[15] Z. Yang, Z. Niu, Y. Lu, Z. Hu, C. C. Han, *Angew. Chem.* **2003**, 115, 1987.

[16] M. Mo, J. C. Yu, L. Zhang, S.-K. A. Li, *Adv. Mater.* **2005**, 17, 756.

[17] L. Wang, Y. Yamauchi, *J. Am. Chem. Soc.* **2013**, 135, 16762.

[18] Y. Chen, H.-R. Chen, J.-L. Shi, *Acc. Chem. Res.* **2014**, 47, 125.

[19] J. Chen, B. Wiley, J. McLellan, Y. Xiong, Z.-Y. Li, Y. Xia, *Nano Lett.* **2005**, 5, 2058.

[20] Y. Yang, J. Liu, Z.-W. Fu, D. Qin, *J. Am. Chem. Soc.* **2014**, 136, 8153.

[21] D. T. Nguyen, K.-S. Kim, *Chem. Eng. J.* **2016**, 286, 266.

[22] Y. Son, Y. Son, M. Choi, M. Ko, S. Chae, N. Park, J. Cho, *Nano Lett.* **2015**, 15, 6914.

[23] M. Eddaoudi, D. F. Sava, J. F. Eubank, K. Adil, V. Guillerm, *Chem. Soc. Rev.* **2015**, 44, 228.

[24] K. J. Gagnon, H. P. Perry, A. Clearfield, *Chem. Rev.* **2012**, 112, 1034.

[25] H. Deng, S. Grunder, K. E. Cordova, C. Valente, H. Furukawa, M. Hmadeh, F. Gándara, A. C. Whalley, Z. Liu, S. Asahina, H. Kazumori, M. O'Keeffe, O. Terasaki, J. F. Stoddart, O. M. Yaghi, *Science* **2012**, 336, 1018.

[26] R. Batten Stuart, R. Champness Neil, X.-M. Chen, J. Garcia-Martinez, S. Kitagawa, L. Öhrström, M. O'Keeffe, M. Paik Suh, J. Reedijk, in *Pure Appl. Chem.*, Vol. 85, 2013, 1715.

[27] Z.-J. Lin, J. Lu, M. Hong, R. Cao, *Chem. Soc. Rev.* **2014**, 43, 5867.

[28] B. Valizadeh, T. N. Nguyen, K. C. Stylianou, *Polyhedron* **2018**, 145, 1.

[29] Y. Bai, Y. Dou, L.-H. Xie, W. Rutledge, J.-R. Li, H.-C. Zhou, *Chem. Soc. Rev.* **2016**, 45, 2327.

[30] G. Xu, P. Nie, H. Dou, B. Ding, L. Li, X. Zhang, *Mater. Today* **2017**, 20, 191.

[31] Y. Cui, B. Li, H. He, W. Zhou, B. Chen, G. Qian, *Acc. Chem. Res.* **2016**, 49, 483.

[32] H.-C. J. Zhou, S. Kitagawa, *Chem. Soc. Rev.* **2014**, 43, 5415.

[33] T. Rodenas, I. Luz, G. Prieto, B. Seoane, H. Miro, A. Corma, F. Kapteijn, I. X. F. X. Llabres, J. Gascon, *Nat. Mater.* **2015**, 14, 48.

[34] X. Li, Y. Liu, J. Wang, J. Gascon, J. Li, B. Van der Bruggen, *Chem. Soc. Rev.* **2017**, 46, 7124.

[35] W. P. Lustig, S. Mukherjee, N. D. Rudd, A. V. Desai, J. Li, S. K. Ghosh, *Chem. Soc. Rev.* **2017**, 46, 3242.

[36] S. Lawson, A. A. Rownaghi, F. Rezaei, *Energy Technol.* **2018**, 6, 694.

[37] J. Lee, J. H. Kwak, W. Choe, *Nat. Commun.* **2017**, 8, 14070.

[38] J. Huo, M. Marcello, A. Garai, D. Bradshaw, *Adv. Mater.* **2013**, 25, 2717.

[39] C. M. Doherty, D. Buso, A. J. Hill, S. Furukawa, S. Kitagawa, P. Falcaro, *Acc. Chem. Res.* **2014**, 47, 396.

[40] X. Cao, C. Tan, M. Sindoro, H. Zhang, *Chem. Soc. Rev.* **2017**, 46, 2660.

[41] Y. V. Kaneti, J. Tang, R. R. Salunkhe, X. Jiang, A. Yu, K. C. Wu, Y. Yamauchi, *Adv. Mater.* **2017**, 29, 1604898.

[42] X. Sun, A. I. O. Suarez, M. Meijerink, T. van Deelen, S. Ould-Chikh, J. Zečević, K. P. de Jong, F. Kapteijn, J. Gascon, *Nat. Commun.* **2017**, 8, 1680.

[43] R. R. Salunkhe, Y. V. Kaneti, J. Kim, J. H. Kim, Y. Yamauchi, *Acc. Chem. Res.* **2016**, 49, 2796.

[44] M. Hu, J. Reboul, S. Furukawa, N. L. Torad, Q. Ji, P. Srinivasu, K. Ariga, S. Kitagawa, Y. Yamauchi, *J. Am. Chem. Soc.* **2012**, 134, 2864.

[45] J. Tang, Y. Yamauchi, *Nat. Chem.* **2016**, 8, 638.

[46] P. Pachfule, D. Shinde, M. Majumder, Q. Xu, *Nat. Chem.* **2016**, 8, 718.

[47] S. Dang, Q.-L. Zhu, Q. Xu, *Nat. Rev. Mater.* **2017**, 3, 17075.

[48] K. Shen, X. Chen, J. Chen, Y. Li, *ACS Catal.* **2016**, 6, 5887.

[49] H. Chen, Z.-G. Gu, S. Mirza, S.-H. Zhang, J. Zhang, *J. Mater. Chem. A* **2018**, 6, 7175.

[50] A. Jayakumar, R. P. Antony, R. Wang, J.-M. Lee, *Small* **2017**, 13, 1603102.

[51] H. D. Mai, K. Rafiq, H. Yoo, *Chem. Eur. J.* **2017**, 23, 5631.

[52]Y. Yang, S. Jin, Z. Zhang, Z. Du, H. Liu, J. Yang, H. Xu, H. Ji, *ACS Appl. Mater. Interfaces* **2017**, 9, 14180.

[53]R. R. Salunkhe, Y. V. Kaneti, Y. Yamauchi, *ACS Nano* **2017**, 11, 5293.

[54] H. Zhang, J. Nai, L. Yu, X. W. Lou, *Joule* **2017**, 1, 77.

[55] H. Yang, X. Wang, *Adv. Mater.* **2018**, 30, 1800743.

[56] X.-C. Xie, K.-J. Huang, X. Wu, *J. Mater. Chem. A* **2018**, 6, 6754.

[57] B. Y. Guan, X. Y. Yu, H. B. Wu, X. W. D. Lou, *Adv. Mater.* **2017**, 29, 1703614.

[58] H. Kim, M. S. Lah, *Dalton Trans.* **2017**, 46, 6146.

[59] H. J. Lee, J.-U. Park, S. Choi, J. Son, M. Oh, *Small* **2013**, 9, 561.

[60] K. Shen, L. Zhang, X. Chen, L. Liu, D. Zhang, Y. Han, J. Chen, J. Long, R. Luque, Y. Li, B. Chen, *Science* **2018**, 359, 206.

[61] M. Pang, A. J. Cairns, Y. Liu, Y. Belmabkhout, H. C. Zeng, M. Eddaoudi, *J. Am. Chem. Soc.* **2013**, 135, 10234.

[62] J. Huo, L. Wang, E. Irran, H. Yu, J. Gao, D. Fan, B. Li, J. Wang, W. Ding, A. M. Amin, C. Li, L. Ma, *Angew. Chem. Int. Ed.* **2010**, 49, 9237.

[63] S.-L. Zhong, R. Xu, L.-F. Zhang, W.-G. Qu, G.-Q. Gao, X.-L. Wu, A.-W. Xu, *J. Mater. Chem.* **2011**, 21, 16574.

[64] I. Lee, S. Choi, H. J. Lee, M. Oh, *Cryst. Growth Des.* **2015**, 15, 5169.

[65] Z. Zhang, Y. Chen, X. Xu, J. Zhang, G. Xiang, W. He, X. Wang, *Angew. Chem. Int. Ed.* **2014**, 53, 429.

[66] Z. Zhang, Y. Chen, S. He, J. Zhang, X. Xu, Y. Yang, F. Nosheen, F. Saleem, W. He, X. Wang, *Angew. Chem. Int. Ed.* **2014**, 53, 12517.

[67] X.-Z. Song, Y.-L. Meng, Z. Tan, L. Qiao, T. Huang, X.-F. Wang, *Inorg. Chem.* **2017**, 56, 13646.

[68] K. Jayaramulu, K. S. Krishna, S. J. George, M. Eswaramoorthy, T. K. Maji, *Chem. Commun.* **2013**, 49, 3937.

[69] M. Hu, Y. Ju, K. Liang, T. Suma, J. Cui, F. Caruso, *Adv. Funct. Mater.* **2016**, 26, 5827.

[70] C. Avci, J. Arinez-Soriano, A. Carne-Sanchez, V. Guillerm, C. Carbonell, I. Imaz, D. Maspoch, *Angew. Chem. Int. Ed.* **2015**, 54, 14417.

[71] W. Liu, J. Huang, Q. Yang, S. Wang, X. Sun, W. Zhang, J. Liu, F. Huo, *Angew. Chem.* **2017**, 129, 5604.

[72] M. Hu, S. Furukawa, R. Ohtani, H. Sukegawa, Y. Nemoto, J. Reboul, S. Kitagawa, Y. Yamauchi, *Angew. Chem. Int. Ed.* **2012**, 51, 984.

[73] X. Wang, J. Feng, Y. Bai, Q. Zhang, Y. Yin, *Chem. Rev.* **2016**, 116, 10983.

[74] J.-U. Park, H. J. Lee, W. Cho, C. Jo, M. Oh, *Adv. Mater.* **2011**, 23, 3161.

[75] H. J. Lee, S. Choi, M. Oh, *Chem. Commun.* **2014**, 50, 4492.

[76] A.-L. Li, F. Ke, L.-G. Qiu, X. Jiang, Y.-M. Wang, X.-Y. Tian, *CrystEngComm* **2013**, 15, 3554.

[77] B. Y. Guan, L. Yu, X. W. D. Lou, *Adv. Sci.* **2017**, 4, 1700247.

[78] F. Zhang, Y. Wei, X. Wu, H. Jiang, W. Wang, H. Li, *J. Am. Chem. Soc.* **2014**, 136, 13963.

[79] F. Ke, L.-G. Qiu, Y.-P. Yuan, X. Jiang, J.-F. Zhu, *J. Mater. Chem.* **2012**, 22, 9497.

[80] W. Tian, H. Hu, Y. Wang, P. Li, J. Liu, J. Liu, X. Wang, X. Xu, Z. Li, Q. Zhao, H. Ning, W. Wu, M. Wu, *ACS Nano* **2018**, 12, 1990.

[81] G. Lu, S. Li, Z. Guo, O. K. Farha, B. G. Hauser, X. Qi, Y. Wang, X. Wang, S. Han, X. Liu, J. S. DuChene, H. Zhang, Q. Zhang, X. Chen, J. Ma, S. C. Loo, W. D. Wei, Y. Yang, J. T. Hupp, F. Huo, *Nat. Chem.* **2012**, 4, 310.

[82] C. H. Kuo, Y. Tang, L. Y. Chou, B. T. Sneed, C. N. Brodsky, Z. Zhao, C. K. Tsung, *J. Am. Chem. Soc.* **2012**, 134, 14345.

[83] J. Tang, R. R. Salunkhe, J. Liu, N. L. Torad, M. Imura, S. Furukawa, Y. Yamauchi, *J. Am. Chem. Soc.* **2015**, 137, 1572.

[84] S. Furukawa, K. Hirai, K. Nakagawa, Y. Takashima, R. Matsuda, T. Tsuruoka, M. Kondo, R. Haruki, D. Tanaka, H. Sakamoto, S. Shimomura, O. Sakata, S. Kitagawa, *Angew. Chem.* **2009**, 121, 1798.

[85] K. Koh, A. G. Wong-Foy, A. J. Matzger, *Chem. Commun.* **2009**, 6162.

[86] K. Hirai, S. Furukawa, M. Kondo, H. Uehara, O. Sakata, S. Kitagawa, *Angew. Chem.* **2011**, 123, 8207.

[87] M. Hu, A. A. Belik, M. Imura, Y. Yamauchi, *J. Am. Chem. Soc.* **2013**, 135, 384.

[88] M. Eddaoudi, J. Kim, N. Rosi, D. Vodak, J. Wachter, M. O'Keeffe, O. M. Yaghi, *Science* **2002**, 295, 469.

[89] L. Y. Chou, P. Hu, J. Zhuang, J. V. Morabito, K. C. Ng, Y. C. Kao, S. C. Wang, F. K. Shieh, C. H. Kuo, C. K. Tsung, *Nanoscale* **2015**, 7, 19408.

[90] D. Cai, B. Liu, D. Wang, L. Wang, Y. Liu, B. Qu, X. Duan, Q. Li, T. Wang, *J. Mater. Chem. A* **2016**, 4, 183.

[91] O. N. Risset, E. S. Knowles, S. Ma, M. W. Meisel, D. R. Talham, *Chem. Mater.* **2013**, 25, 42.

[92] X. Y. Liu, F. Zhang, T. W. Goh, Y. Li, Y. C. Shao, L. Luo, W. Huang, Y. T. Long, L. Y. Chou, C. K. Tsung, *Angew. Chem. Int. Ed.* **2018**, 57, 2110.

[93] J. Yang, F. Zhang, H. Lu, X. Hong, H. Jiang, Y. Wu, Y. Li, *Angew. Chem. Int. Ed.* **2015**, 54, 10889.

[94] C. Rösler, A. Aijaz, S. Turner, M. Filippousi, A. Shahabi, W. Xia, G. Van Tendeloo, M. Muhler, R. A. Fischer, *Chem-Eur. J.* **2016**, 22, 3304.

[95] Y. Chuan Tan, H. Chun Zeng, *Chem. Commun.* **2016**, 52, 11591.

[96] Y. M. Chen, L. Yu, X. W. Lou, *Angew. Chem. Int. Ed.* **2016**, 55, 5990.

[97] L. Yu, J. F. Yang, X. W. Lou, *Angew. Chem. Int. Ed.* **2016**, 55, 13422.

[98] E. Leontidis, *Curr. Opin. Colloid Interface Sci.* **2002**, 7, 81.

[99] Y. C. Tan, H. C. Zeng, *Adv. Funct. Mater.* **2017**, 27, 1703765.

[100] Z. Zhu, C. Han, T.-T. Li, Y. Hu, J. Qian, S. Huang, *CrystEngComm* **2018**, 20, 3812.

[101] G. Zhan, H. C. Zeng, *Chem. Commun.* **2016**, 53, 72.

[102] Y. Liu, W. Zhang, S. Li, C. Cui, J. Wu, H. Chen, F. Huo, *Chem. Mater.* **2014**, 26, 1119.

[103] M. Lanchas, D. Vallejo-Sanchez, G. Beobide, O. Castillo, A. T. Aguayo, A. Luque, P. Roman, *Chem. Commun.* **2012**, 48, 9930.

[104] S. Furukawa, J. Reboul, S. Diring, K. Sumida, S. Kitagawa, *Chem. Soc. Rev.* **2014**, 43, 5700.

[105] G.-Y. Jeong, R. Ricco, K. Liang, J. Ludwig, J.-O. Kim, P. Falcaro, D.-P. Kim, *Chem. Mater.* **2015**, 27, 7903.

[106] R. Ameloot, F. Vermoortele, W. Vanhove, M. B. Roeffaers, B. F. Sels, D. E. De Vos, *Nat. Chem.* **2011**, 3, 382.

[107] Y. Yang, F. Wang, Q. Yang, Y. Hu, H. Yan, Y. Z. Chen, H. Liu, G. Zhang, J. Lu, H. L. Jiang, H. Xu, *ACS Appl. Mater. Interfaces* **2014**, 6, 18163.

[108] R. McHale, Y. Liu, N. Ghasdian, N. S. Hondow, S. Ye, Y. Lu, R. Brydson, X. Wang, *Nanoscale* **2011**, 3, 3685.

[109] G. Liang, J. Xu, X. Wang, *J. Am. Chem. Soc.* **2009**, 131, 5378.

[110] R. McHale, N. Ghasdian, Y. Liu, M. B. Ward, N. S. Hondow, H. Wang, Y. Miao, R. Brydson, X. Wang, *Chem. Commun.* **2010**, 46, 4574.

[111] A. Carne-Sanchez, I. Imaz, M. Cano-Sarabia, D. Maspoch, *Nat. Chem.* **2013**, 5, 203.

[112] S. Tanaka, R. Miyashita, *ACS Omega* **2017**, 2, 6437.

[113] G. C. Li, P. F. Liu, R. Liu, M. Liu, K. Tao, S. R. Zhu, M. K. Wu, F. Y. Yi, L. Han, *Dalton Trans.* **2016**, 45, 13311.

[114] D. P. Wang, H. C. Zeng, *Chem. Mater.* **2011**, 23, 4886.

[115] J. Li, H. C. Zeng, *J. Am. Chem. Soc.* **2007**, 129, 15839.

[116] H. C. Zeng, *Curr. Nanosci.* **2007**, 3, 177.

[117] C. C. Yec, H. C. Zeng, *J. Mater. Chem. A* **2014**, 2, 4843.

[118] J. V. Aleman, A. V. Chadwick, J. He, M. Hess, K. Horie, R. G. Jones, P. Kratochvíl, I. Meisel, I. Mita, G. Moad, S. Penczek, R. F. T. Stepto, in *Pure Appl. Chem.*, Vol. 79, 2007, 1801.

[119] X. Xu, F. Nosheen, X. Wang, *Chem. Mater.* **2016**, 28, 6313.

[120] F. Zou, X. Hu, Z. Li, L. Qie, C. Hu, R. Zeng, Y. Jiang, Y. Huang, *Adv. Mater.* **2014**, 26, 6622.

[121] S. Jung, W. Cho, H. J. Lee, M. Oh, *Angew. Chem.* **2009**, 121, 1487.

[122] T. He, X. Xu, B. Ni, H. Lin, C. Li, W. Hu, X. Wang, *Angew. Chem. Int. Ed.* **2018**, 57, 10148.

[123] Q. Zhang, W. Wang, J. Goebl, Y. Yin, *Nano Today* **2009**, 4, 494.

[124] A. J. Howarth, Y. Liu, P. Li, Z. Li, T. C. Wang, J. T. Hupp, O. K. Farha, *Nat. Rev. Mater.* **2016**, 1, 15018.

[125] L. Han, X. Y. Yu, X. W. Lou, *Adv. Mater.* **2016**, 28, 4601.

[126] V. Ganesan, J. Kim, *Mater. Lett.* **2018**, 223, 49.

[127] M. Hu, A. A. Belik, M. Imura, K. Mibu, Y. Tsujimoto, Y. Yamauchi, *Chem. Mater.* **2012**, 24, 2698.

[128] M. Wu, C. Li, J. Zhao, Y. Ling, R. Liu, *Dalton Trans.* **2018**, 47, 7812.

[129] W. Zhang, X. Jiang, Y. Zhao, A. Carne-Sanchez, V. Malgras, J. Kim, J. H. Kim, S. Wang, J. Liu, J. S. Jiang, Y. Yamauchi, M. Hu, *Chem. Sci.* **2017**, 8, 3538.

[130] U. Sen, M. Erkartal, C.-W. Kung, V. Ramani, J. T. Hupp, O. K. Farha, *ACS Appl. Mater. Interfaces* **2016**, 8, 23015.

[131] H. Ejima, J. J. Richardson, K. Liang, J. P. Best, M. P. van Koeverden, G. K. Such, J. Cui, F. Caruso, *Science* **2013**, 341, 154.

[132] J. Guo, Y. Ping, H. Ejima, K. Alt, M. Meissner, J. J. Richardson, Y. Yan, K. Peter, D. von Elverfeldt, C. E. Hagemeyer, F. Caruso, *Angew. Chem.* **2014**, 126, 5652.

[133] X. Song, L. Guo, X. Liao, J. Liu, J. Sun, X. Li, *Small* **2017**, 13, 1700238.

[134] J. A. Boissonnault, A. G. Wong-Foy, A. J. Matzger, *J. Am. Chem. Soc.* **2017**, 139, 14841.

[135] M. Kim, J. F. Cahill, H. Fei, K. A. Prather, S. M. Cohen, *J. Am. Chem. Soc.* **2012**, 134, 18082.

[136] B. J. Burnett, P. M. Barron, C. Hu, W. Choe, *J. Am. Chem. Soc.* **2011**, 133, 9984.

[137] W. Cho, Y. H. Lee, H. J. Lee, M. Oh, *Adv. Mater.* **2011**, 23, 1720.

[138] W. Ahn, M. G. Park, D. U. Lee, M. H. Seo, G. Jiang, Z. P. Cano, F. M. Hassan, Z. Chen, *Adv. Funct. Mater.* **2018**, 28, 1802129.

[139] X. Wang, L. Yu, B. Y. Guan, S. Song, X.W.Lou, *Adv. Mater.* **2018**, 30, 1801211.

[140] L. Zhang, H. B. Wu, X. W. Lou, *J. Am. Chem. Soc.* **2013**, 135, 10664.

[141] Z. F. Huang, J. Song, K. Li, M. Tahir, Y. T. Wang, L. Pan, L. Wang, X. Zhang, J. J. Zou, *J. Am. Chem. Soc.* **2016**, 138, 1359.

[142] Y. Guo, J. Tang, Z. Wang, Y.-M. Kang, Y. Bando, Y. Yamauchi, *Nano Energy* **2018**, 47, 494.

[143] Y. Guo, J. Tang, H. Qian, Z. Wang, Y. Yamauchi, *Chem. Mater.* **2017**, 29, 5566.

[144] Z. Jiang, H. Sun, Z. Qin, X. Jiao, D. Chen, *Chem. Commun.* **2012**, 48, 3620.

[145] S. Wang, B. Y. Guan, Y. Lu, X. W. D. Lou, *J. Am. Chem. Soc.* **2017**, 139, 17305.

[146] P. Zhang, B. Y. Guan, L. Yu, X. W. Lou, *Chem* **2018**, 4, 162.

[147] X. Y. Yu, L. Yu, H. B. Wu, X. W. Lou, *Angew. Chem. Int. Ed.* **2015**, 54, 5331.

[148] Y. Lu, L. Yu, M. Wu, Y. Wang, X. W. D. Lou, *Adv. Mater.* **2018**, 30, 1702875.

[149] Z.-W. Zhao, T. Wen, K. Liang, Y.-F. Jiang, X. Zhou, C.-C. Shen, A.-W. Xu, *ACS Appl. Mater. Interfaces* **2017**, 9, 3757.

[150] Y. Zhang, H. Chen, C. Guan, Y. Wu, C. Yang, Z. Shen, Q. Zou, *ACS Appl. Mater. Interfaces* **2018**, 10, 18440.

[151] Y. Fang, X.-Y. Yu, X. W. Lou, *Adv. Mater.* **2018**, 30, 1706668.

[152] M. K. Aslam, S. S. A. Shah, S. Li, C. Chen, *J. Mater. Chem. A* **2018**, 6, 14083.

[153] X. Y. Yu, Y. Feng, Y. Jeon, B. Guan, X. W. Lou, U. Paik, *Adv. Mater.* **2016**, 28, 9006.

[154] F. Lyu, Y. Bai, Z. Li, W. Xu, Q. Wang, J. Mao, L. Wang, X. Zhang, Y. Yin, *Adv. Funct. Mater.* **2017**, 27, 1702324.

[155] C. Guan, X. M. Liu, W. N. Ren, X. Li, C. W. Cheng, J. Wang, *Adv. Energy Mater.* **2017**, 7, 1602391.

[156] G. Yilmaz, K. M. Yam, C. Zhang, H. J. Fan, G. W. Ho, *Adv. Mater.* **2017**, 29, 1606814.

[157] Z. Jiang, Z. Li, Z. Qin, H. Sun, X. Jiao, D. Chen, *Nanoscale* **2013**, 5, 11770.

[158] C. Sun, J. Yang, X. Rui, W. Zhang, Q. Yan, P. Chen, F. Huo, W. Huang, X. Dong, *J. Mater. Chem. A* **2015**, 3, 8483.

[159] Y.-M. Jo, T.-H. Kim, C.-S. Lee, K. Lim, C. W. Na, F. Abdel-Hady, A. A. Wazzan, J.-H. Lee, *ACS Appl. Mater. Interfaces* **2018**, 10, 8860.

[160] J. Zhang, Z. Li, Y. Chen, S. Gao, X. W. Lou, *Angew. Chem. Int. Ed.* **2018**, 57, 10944.

[161] J. Guan, F. Mou, Z. Sun, W. Shi, *Chem. Commun.* **2010**, 46, 6605.

[162] L. Shen, L. Yu, X.-Y. Yu, X. Zhang, X. W. Lou, *Angew. Chem. Int. Ed.* **2015**, 54, 1868.

[163] J. Li, J. Wang, X. Liang, Z. Zhang, H. Liu, Y. Qian, S. Xiong, *ACS Appl. Mater. Interfaces* **2014**, 6, 24.

[164] B. Y. Guan, L. Yu, X. W. Lou, *Angew. Chem. Int. Ed.* **2017**, 56, 2386.

[165] B. Y. Guan, A. Kushima, L. Yu, S. Li, J. Li, X. W. D. Lou, *Adv. Mater.* **2017**, 29, 1605902.

[166] A. A. Ensafi, S. E. Moosavifard, B. Rezaei, S. K. Kaverlavani, *J. Mater. Chem. A* **2018**, 6, 10497.

[167] L. L. Wu, Z. Wang, Y. Long, J. Li, Y. Liu, Q. S. Wang, X. Wang, S. Y. Song, X. Liu, H. J. Zhang, *Small* **2017**, 13, 1604270.

[168] G. Zhan, H. C. Zeng, *Chem. Mater.* **2017**, 29, 10104.

[169] W. Guo, W. Sun, Y. Wang, *ACS Nano* **2015**, 9, 11462.

[170] Q.-L. Zhu, P. Pachfule, P. Strubel, Z. Li, R. Zou, Z. Liu, S. Kaskel, Q. Xu, *Energy Storage Mater.* **2018**, 13, 72.

[171] Q. L. Zhu, W. Xia, T. Akita, R. Zou, Q. Xu, *Adv. Mater.* **2016**, 28, 6391.

[172] L. Han, P. Tang, Á. Reyes-Carmona, B. Rodríguez-García, M. Torréns, J. R. Morante, J. Arbiol, J. R. Galan-Mascaros, *J. Am. Chem. Soc.* **2016**, 138, 16037.

[173] S. Wang, L. Shang, L. Li, Y. Yu, C. Chi, K. Wang, J. Zhang, R. Shi, H. Shen, G. I. N. Waterhouse, S. Liu, J. Tian, T. Zhang, H. Liu, *Adv. Mater.* **2016**, 28, 8379.

[174] C. Liu, X. Huang, J. Wang, H. Song, Y. Yang, Y. Liu, J. Li, L. Wang, C. Yu, *Adv. Funct. Mater.* **2018**, 28, 1705253.

[175] S. Yang, L. Peng, P. Huang, X. Wang, Y. Sun, C. Cao, W. Song, *Angew. Chem. Int. Ed.* **2016**, 55, 4016.

[176] H. Yang, S. J. Bradley, A. Chan, G. I. N. Waterhouse, T. Nann, P. E. Kruger, S. G. Telfer, *J. Am. Chem. Soc.* **2016**, 138, 11872.

[177] G. Huang, D. Yin, F. Zhang, Q. Li, L. Wang, *Inorg. Chem.* **2017**, 56, 9794.

[178] H. Yang, P. E. Kruger, S. G. Telfer, *Inorg. Chem.* **2015**, 54, 9483.

[179] Z. Li, Y. Fang, J. Zhang, X. W. Lou, *Adv. Mater.* **2018**, 30, 1800525.

[180] G. Huang, L. Zhang, F. Zhang, L. Wang, *Nanoscale* **2014**, 6, 5509.

[181] G. Huang, F. Zhang, L. Zhang, X. Du, J. Wang, L. Wang, *J. Mater. Chem. A* **2014**, 2, 8048.

[182] J. Tang, R. R. Salunkhe, J. Liu, N. L. Torad, M. Imura, S. Furukawa, Y. Yamauchi, *J. Am. Chem. Soc.* **2015**, 137, 1572.

[183] Y. Pan, K. Sun, S. Liu, X. Cao, K. Wu, W.-C. Cheong, Z. Chen, Y. Wang, Y. Li, Y. Liu, D. Wang, Q. Peng, C. Chen, Y. Li, *J. Am. Chem. Soc.* **2018**, 140, 2610.

[184] B. Y. Guan, Y. Lu, Y. Wang, M. Wu, X. W. D. Lou, *Adv. Funct. Mater.* **2018**, 28, 1706738.

[185] S. Liu, Z. Wang, S. Zhou, F. Yu, M. Yu, C.-Y. Chiang, W. Zhou, J. Zhao, J. Qiu, *Adv. Mater.* **2017**, 29, 1700874.

[186] W. Zhang, X. Jiang, X. Wang, Y. V. Kaneti, Y. Chen, J. Liu, J.-S. Jiang, Y. Yamauchi, M. Hu, *Angew. Chem. Int. Ed.* **2017**, 56, 8435.

[187] L. Chen, J. Bai, C. Wang, Y. Pan, M. Scheer, X. You, *Chem. Commun.* **2008**, 1581.

[188] T. Liu, P. Zhao, X. Hua, W. Luo, S. Chen, G. Cheng, *J. Mater. Chem. A* **2016**, 4, 11357.

[189] P. Su, H. Xiao, J. Zhao, Y. Yao, Z. Shao, C. Li, Q. Yang, *Chem. Sci.* **2013**, 4, 2941.

[190] L. Qing, X. Ping, G. Wei, M. Shuguo, Z. Guoqi, C. Ruiguo, C. Jaephil, W. Hsing-Lin, W. Gang, *Adv. Mater.* **2014**, 26, 1378.

[191] J. Meng, C. Niu, L. Xu, J. Li, X. Liu, X. Wang, Y. Wu, X. Xu, W. Chen, Q. Li, Z. Zhu, D. Zhao, L. Mai, *J. Am. Chem. Soc.* **2017**, 139, 8212.

[192] H. Zhou, D. He, A. I. Saana, J. Yang, Z. Wang, J. Zhang, Q. Liang, S. Yuan, J. Zhu, S. Mu, *Nanoscale* **2018**, 10, 6147.

[193] B. Y. Xia, Y. Yan, N. Li, H. B. Wu, X. W. Lou, X. Wang, *Nat. Energy* **2016**, 1, 15006.

[194] L. Qing, P. Hengyu, H. Drew, C. Ruiguo, Z. Guoqi, L. Haifeng, W. Kangbing, C. Jaephil, W. Gang, *Small* **2015**, 11, 1443.

[195] Z. Jiang, W. Lu, Z. Li, K. H. Ho, X. Li, X. Jiao, D. Chen, *J. Mater. Chem. A* **2014**, 2, 8603.

[196] B. Y. Guan, X. W. David Lou, *Small Methods* **2017**, 1, 1700158.

[197] F. Yongjin, Y. Xin-Yao, L. X. Wen, *Adv. Mater.* **2018**, 30, 1706668.

[198] L. Zhang, H. B. Wu, S. Madhavi, H. H. Hng, X. W. Lou, *J. Am. Chem. Soc.* **2012**, 134, 17388.

[199] C. Niu, M. Huang, P. Wang, J. Meng, X. Liu, X. Wang, K. Zhao, Y. Yu, Y. Wu, C. Lin, L. Mai, *Nano Res.* **2016**, 9, 128.

[200] V. Soundharrajan, B. Sambandam, J. Song, S. Kim, J. Jo, S. Kim, S. Lee, V. Mathew, J. Kim, *ACS Appl. Mater. Interfaces* **2016**, 8, 8546.

[201] P. Zhang, B. Y. Guan, L. Yu, X. W. D. Lou, *Angew. Chem. Int. Ed.* **2017**, 56, 7141.

[202] R. Ma, Y. Zhou, Y. Chen, P. Li, Q. Liu, J. Wang, *Angew. Chem. Int. Ed.* **2015**, 54, 14723.

[203] Y. Zhong, X. Xia, F. Shi, J. Zhan, J. Tu, H. J. Fan, *Adv. Sci.* **2016**, 3, 1500286.

[204] J. Huang, Y. Li, Y. Xia, J. Zhu, Q. Yi, H. Wang, J. Xiong, Y. Sun, G. Zou, *Nano Res.* **2017**, 10, 1010.

[205] M. Gaab, N. Trukhan, S. Maurer, R. Gummaraju, U. Müller, *Microporous Mesoporous Mater.* **2012**, 157, 131.

[206] D. DeSantis, J. A. Mason, B. D. James, C. Houchins, J. R. Long, M. Veenstra, *Energ. Fuel* **2017**, 31, 2024.

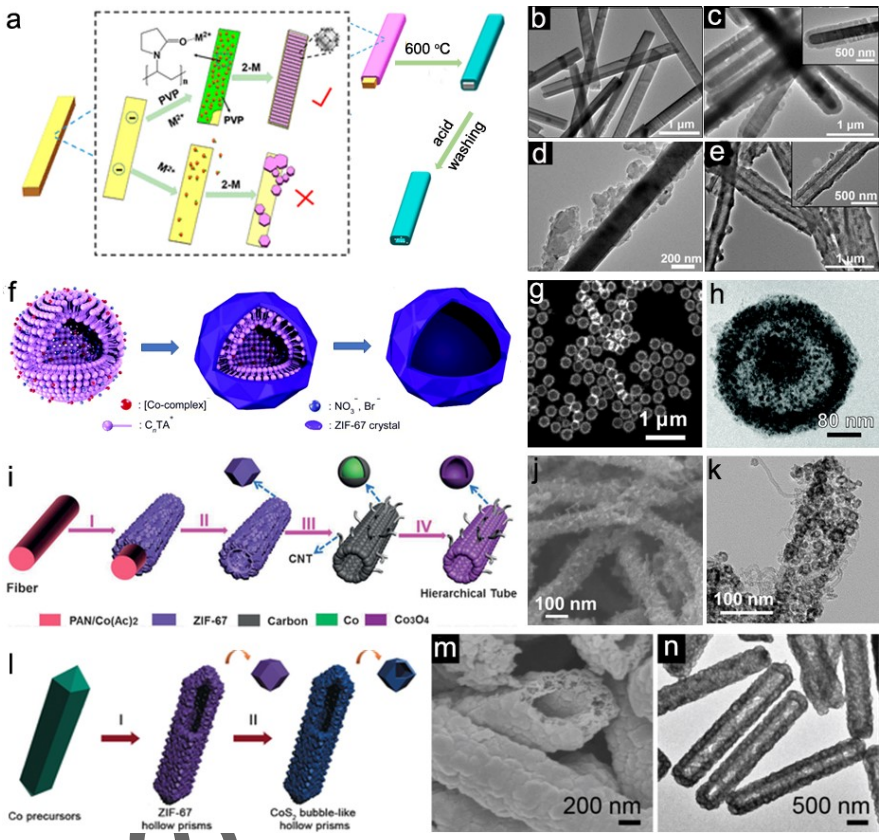

Figure 1. a) Schematic diagram of the controlled synthesis of hollow MoO_2/carbon nanotubes assisted by PVP, b–e) Transmission electron microscopy (TEM) images of as-prepared MoO_3 nanorods (b), MoO_3@BMZIF mediates assisted by PVP (c), BMZIF-coated MoO_3 nanorods without addition of PVP (d), and hollow MoO_2/carbon nanotubes (e). a–e) Reproduced with permission.[80] Copyright 2018, American Chemical Society. f) Simplified illustration of the growth mechanism of ZIF-67-HS by electrostatic-interaction-induced self-assembly. g,h) HAADF-STEM image of ZIF-67-HS (g) and TEM image (h) of Co/C-YS nanocomposite. g,h) Reproduced with permission.[95] Copyright 2016, Royal Society of Chemistry. i) Schematic diagram of the synthesis of hierarchical CNT/Co_3O_4 microtubes by using PAN/$Co(Ac)_2$ as both template and precursors. j) Field-emission scanning electron microscopy (FESEM) images (j) and TEM images (k) of the as-prepared hierarchical CNT/Co_3O_4 microtubes. j,k) Reproduced with permission.[96] Copyright 2016, Wiley-VCH. l) Schematic diagram on the synthesis of CoS_2 hollow prisms using Co-containing prims as both templates and precursors. m,n) FESEM images (m) and TEM images (n) of as-prepared hierarchical CoS_4 hollow prisms. m,n) Reproduced with permission.[97] Copyright 2016, Wiley-VCH.

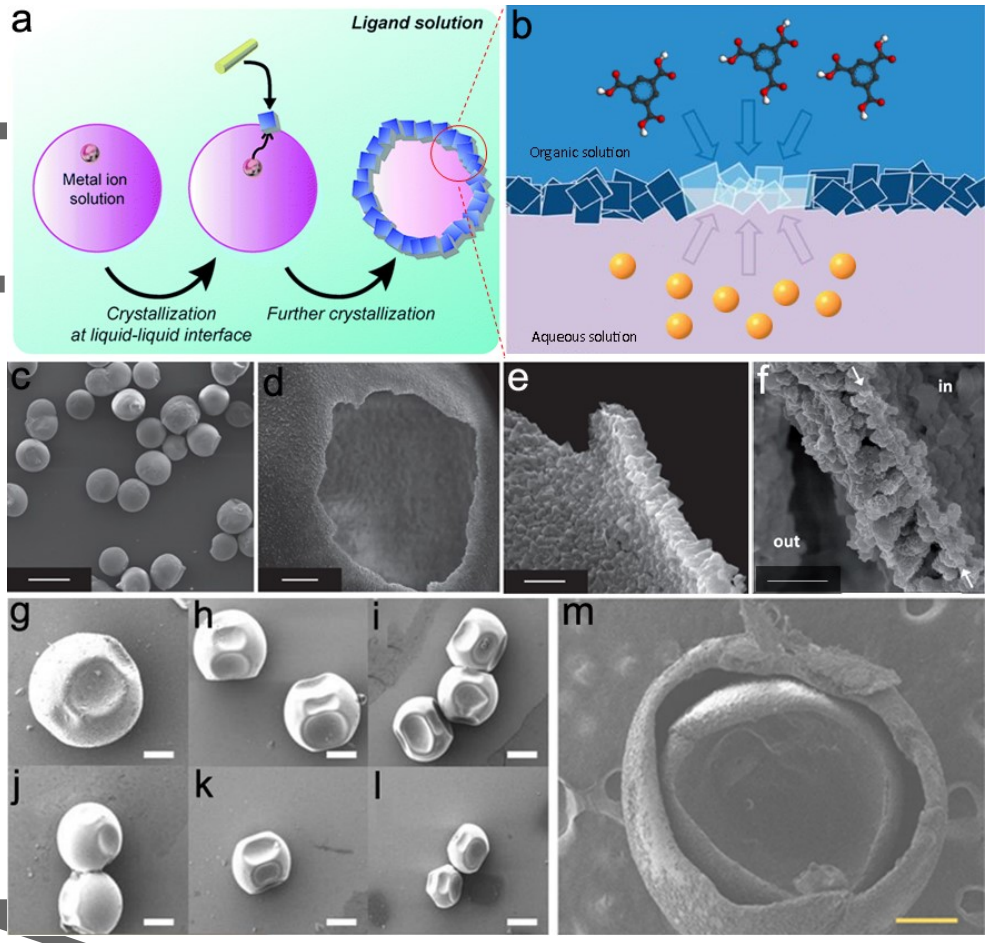

Figure 2. a) Schematic illustration of the synthesis of hollow MOF architectures via liquid–liquid interfacial reaction protocol by using immiscible liquid components. Reproduced with permission.[104] Copyright 2014, Royal Society of Chemistry. b) Schematic illustration of the liquid–liquid interface reaction in the case of $[Cu_3(BTC)_2]$. c–f) SEM images of as-prepared hollow $[Cu_3(BTC)_2]$ capsules , scale bar 500 µm (c), a capsule crushed with a needle tip showing its hollow interior, scale bar 25 µm (d), across-sectional view of the capsule wall, showing its thin and uniform thickness, scale bar 2 µm (e); and a cross-sectional view of a capsule wall prepared when 20 wt% ethanol is added to the aqueous phase, scale bar 2.5 µm (f). b–f) Reproduced with permission.[106] Copyright 2011, Nature Publishing Group. g–l) SEM images of a monodisperse MIL-88A sphere with different sizes obtained by varying flow rates and capillary diameters, scale bar 100 µm. m) SEM image of as-prepared MIL-88A double-shelled hollow capsules, scale bar 100 µm. g–m) Reproduced with permission.[105] Copyright 2015, American Chemical Society.

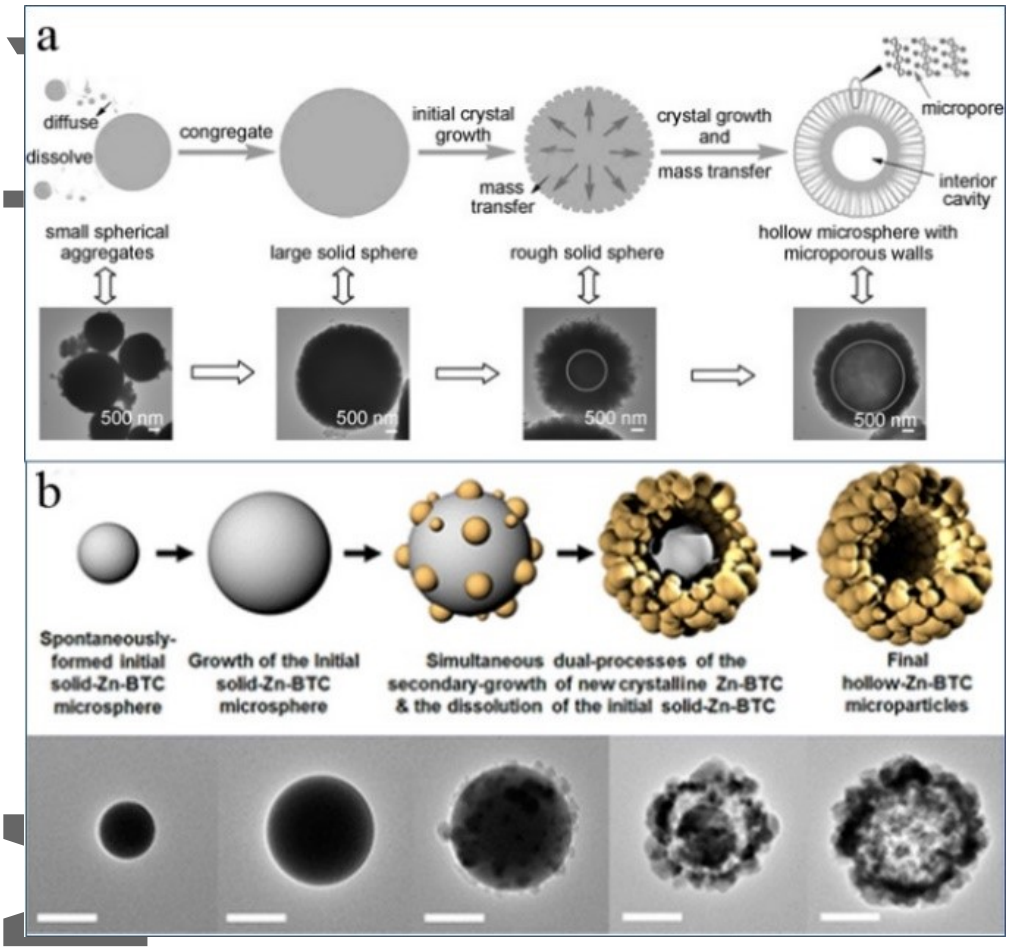

Figure 3. a) Schematic diagram of Ostwald ripening process in the formation of Fe-Fc-HCPS and the corresponding TEM images. Reproduced with permission.[62] Copyright 2009, Wiley-VCH. b) Schematic diagram for the synthesis of hollow Zn-BTC microparticles metastable core-directed secondary growth. Scale bars are 1 μm. Reproduced with permission.[64] Copyright 2015, American Chemical Society.

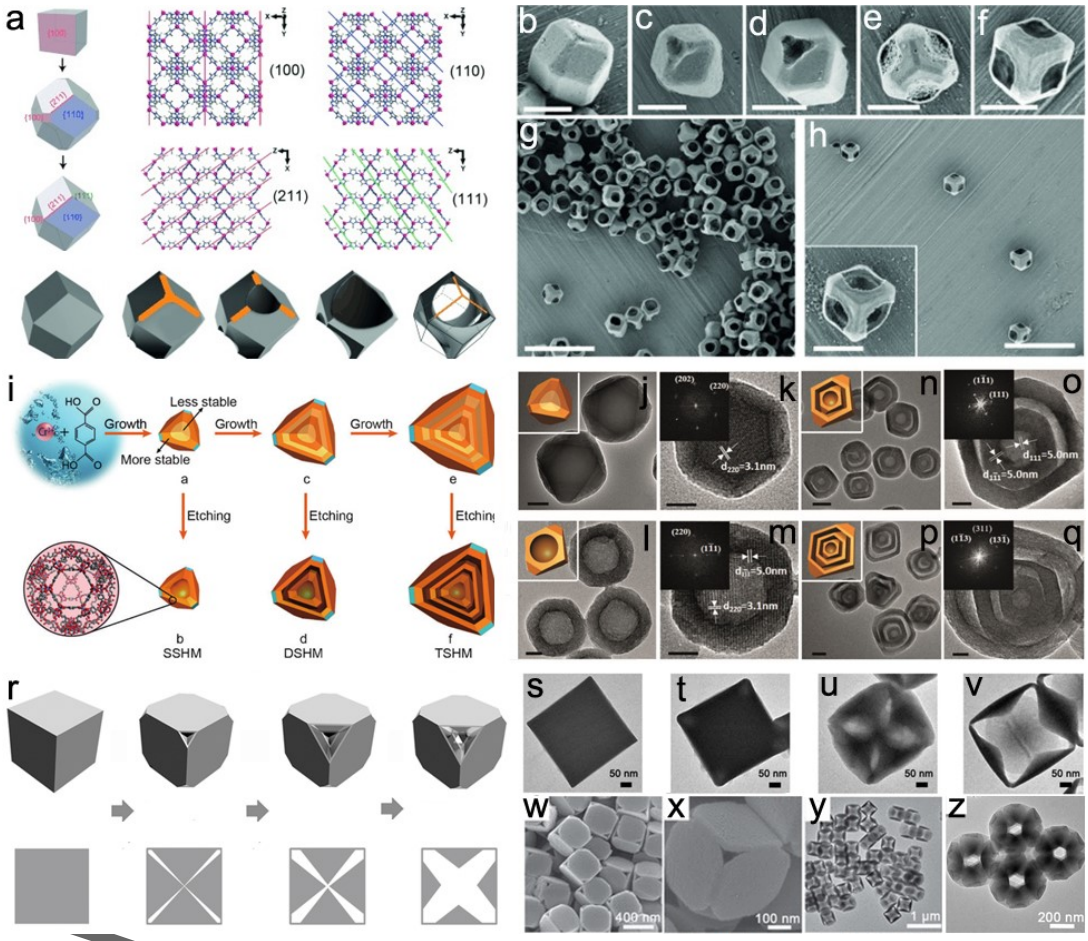

Figure 4. a) Schematic representations of the crystal structure of the exposed crystallographic planes of ZIF crystals and illustration of the morphology changes during the etching reactions. b–f) Corresponding SEM images of morphology changes in ZIF crystals during the etching process. g–k) Representative FE-SEM images of hollow ZIF microboxes. Scale bars: 5 μm (g,h) and 1 μm (b–f, h inset). b–k) Reproduced with permission.[70] Copyright 2015, Wiley-VCH. i) Schematic representation of the fabrication process of multishell hollow MIL-101. j–q) TEM and HRTEM images of solid MIL-101 (j,k), single-shelled hollow MIL-101 (l,m), double-shelled hollow MIL-101 (n,o), and triple-shelled hollow MIL-101 (p,q). Scale bars: 50 nm (j–m,o,q) and 200 nm (n,p). The insets in (k), (m), (o), and (q) show the corresponding FFT patterns. i–q) Reproduced with permission.[71] Copyright 2017, Wiley-VCH. r) Schematic illustration of the formation process of Ni–Co PBA cages. s–v) TEM images of the as-prepared products by etching Ni–Co PBA cubes for 0 h (s), 0.5 h (t), 2 h (u), and 6 h (v) in ammonia at room temperature. w–z) Typical FESEM (w,x) and TEM (y,z) images of the as-prepared Ni–Co PBA cages. s–z) Reproduced with permission.[125] Copyright 2016, Wiley-VCH.

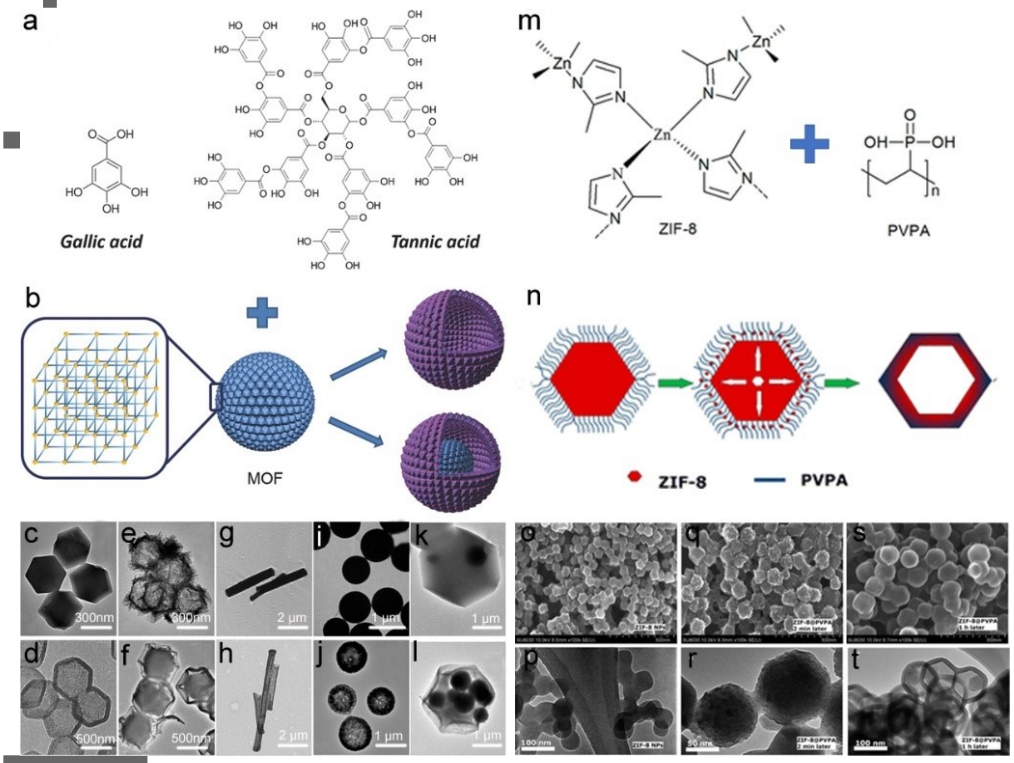

Figure 5. a) Molecular structures of tannic acid and gallic acid. b) Schematic representation of the etching reactions to create voids inside MOFs. c–e) TEM images of ZIF-8 crystals (c) and hollow ZIF-8 etched by TA (d) or GA (e). f) TEM images of ZIF-8 crystals partially etched by TA. g,h) TEM images of MIL-68 crystals (g) and hollow MIL-68 etching by TA (h). i,j) TEM images of Tb-CP spheres (i) and hollow Tb-CP spheres etched by GA (j). k,l) TEM images of yolk–shell Fe_3O_4@ZIF-8 (k) and hollow yolk–shell Fe_3O_4@ZIF-8 etched by TA (l). a–l) Reproduced with permission.[69] Copyright 2016, Wiley-VCH. m) Molecular structures of ZIF-8 and PVPA. n) Proposed schematic diagram for the etching process of ZIF-8 by PVPA. o,p) SEM image (o) and TEM image (p) of ZIF-8 crystals. q–t) SEM image (q) and TEM image (r) of ZIF-8@PVPA NPs after reaction for 2 min, and SEM image (s) and TEM image (t) of ZIF@PVPA hollow nanostructures after reaction for 60 min. m–t) Reproduced with permission.[130] Copyright 2016, American Chemical Society.

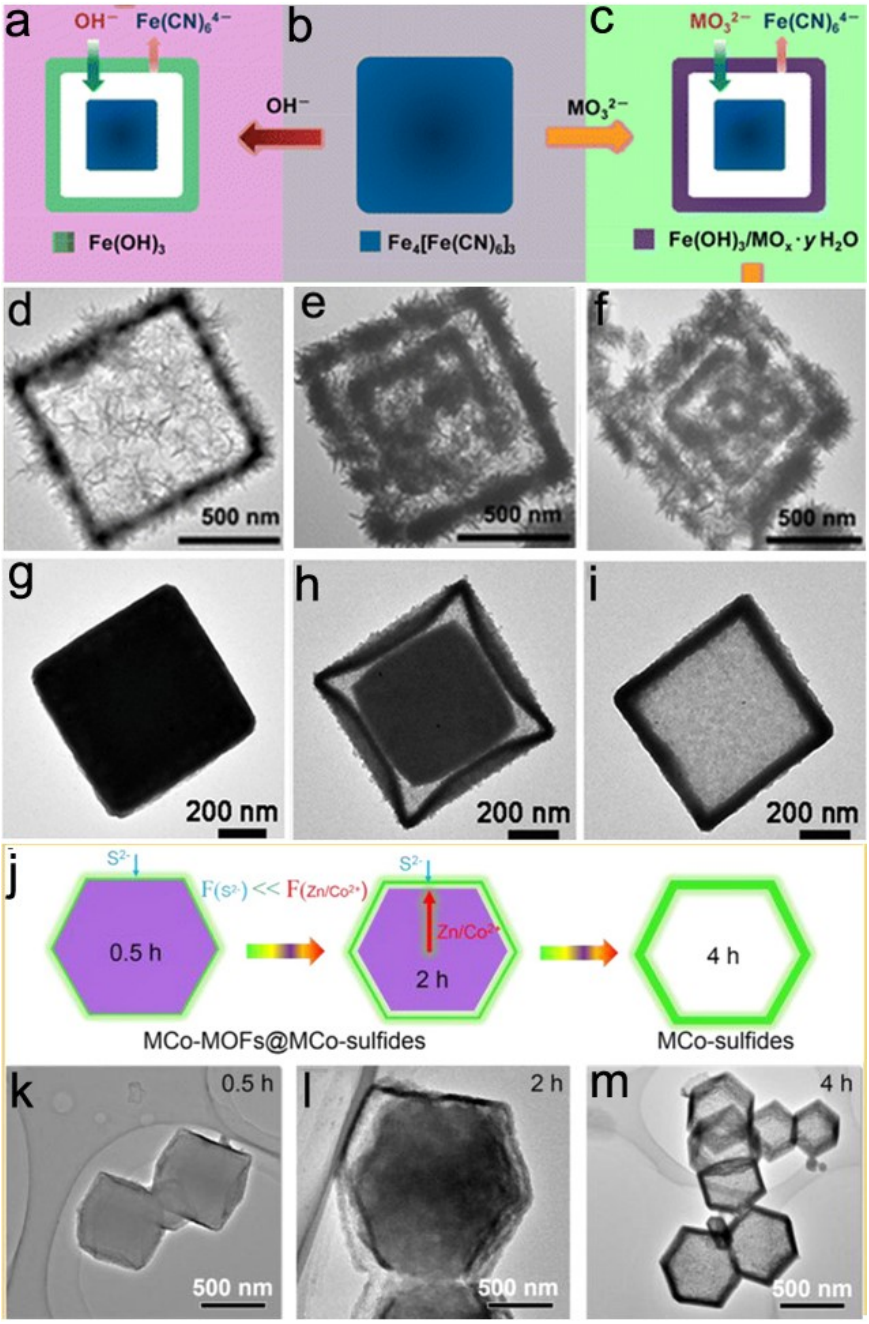

Figure 6. a–c) Schematic illustration of the ion-exchange reaction between PB crystals and various bases. d–f) TEM images of as-prepared hierarchical $Fe(OH)_3$ microboxes with single-shelled (d) and multiple-shelled (e,f) structures after reaction under hydrothermal conditions. a–f) Reproduced with permission.[140] Copyright 2016, American Chemical Society. g–i) TEM images of hollow $Co_3V_2O_8$ prepared with different VOT concentrations: 0 μL (g), 50 μL (h), and 120 μL (i). g–i) Reproduced with permission.[148] Copyright 2018, Wiley-VCH. j–m) Time-dependent formation of hollow

$Zn_{0.30}Co_{2.70}S_4$ polyhedra. j–m) Reproduced with permission.[141] Copyright 2016, American Chemical Society.

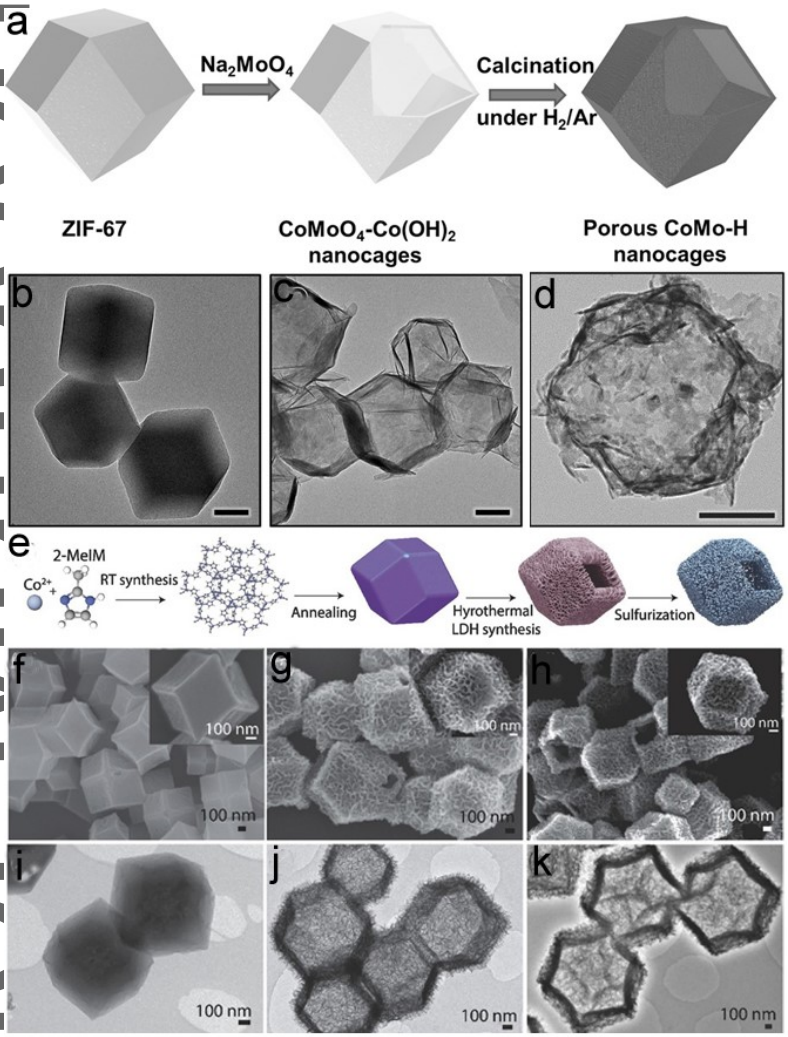

Figure 7. a) Schematic description of the synthesis of CoO-MoO_2 nanocages. b–d) TEM images of ZIF-67 (b), $CoMoO_4$–$Co(OH)_2$ (c), and CoMo-H (d). Scale bars: 100 nm in (g–i). a–d) Reproduced with permission. [154] Copyright 2017, Wiley-VCH. e) Schematic diagrams for the synthesis of the hollow NiCo-LDH/Co_9S_8 hybrid. f–h) FE-SEM images of ZIF-67-C (f), C/LDH (g), and C/LDH/S (h) polyhedrons in low and high (inset) magnification. i–k) Corresponding TEM images of ZIF-67-C (i), C/LDH (j), and C/LDH/S (k) polyhedrons. e–k) Reproduced with permission.[156] Copyright 2017, Wiley-VCH.

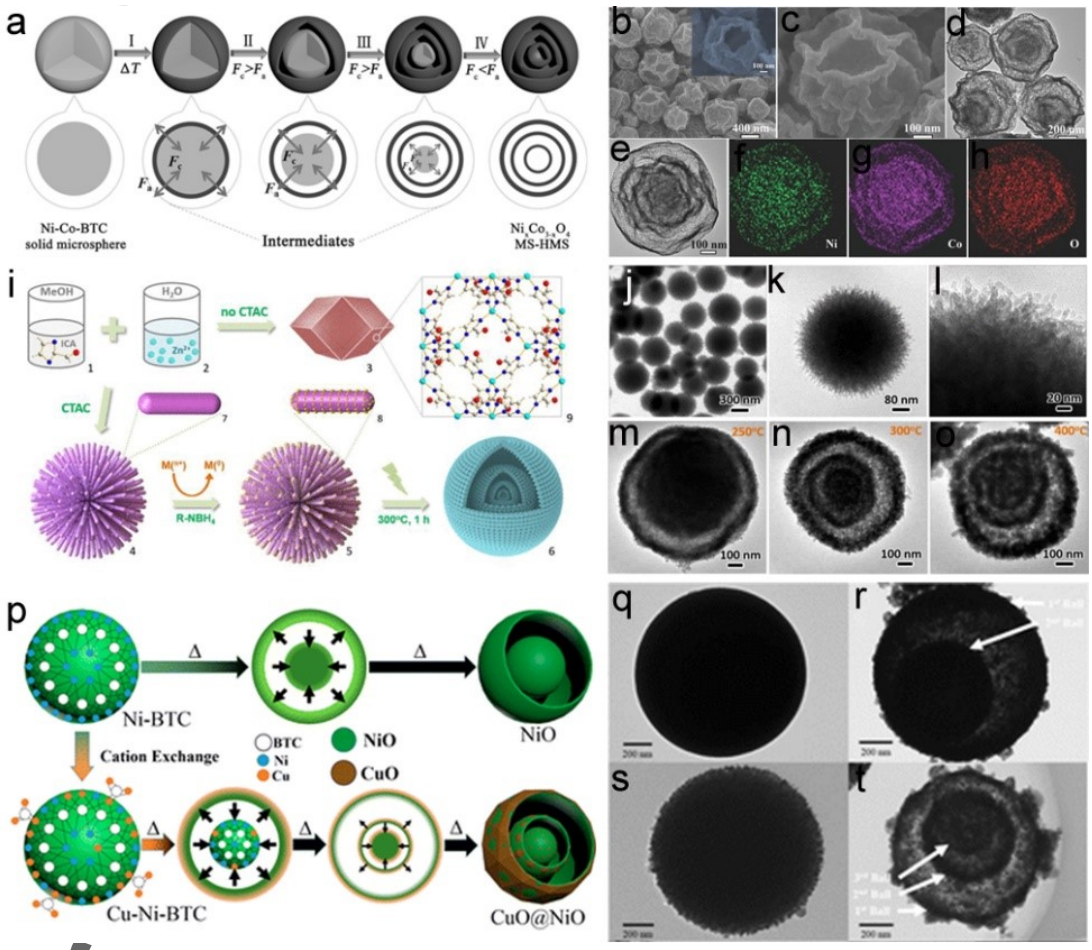

Figure 8. a) Schematic diagram of the synthesis of $Ni_xCo_{3-x}O_4$ MS-HMSs. b–h) Structural characterization of $Ni_xCo_{3-x}O_4$–0.1 MS–HMSs: FESEM images (b,c), TEM images (d,e), and EDS elemental mapping images (f–h). a–h) Reproduced with permission.[167] Copyright 2017, Wiley-VCH. i) Schematic representation of the synthesis of a_mZIF-90/M particles and their pyrolysis to multishelled CuO/ZnO. j–o) TEM images of a_mZIF-90 (j–l) and as-prepared multishelled CuO/ZnO spheres obtained by the controlled pyrolysis of a_mZIF-90/Cu at different temperatures in air (m–o). i–o) Reproduced with permission.[168] Copyright 2017, American Chemical Society. p) Schematic diagram of the thermal decomposition of Ni–BTC and Cu–Ni–BTC fabricated via a cation-exchange process. q–t) TEM images of Ni–BTC (q), NiO (r), Cu–Ni–BTC (s), and CuO@NiO (t). p–t) Reproduced with permission.[169] Copyright 2015, American Chemical Society.

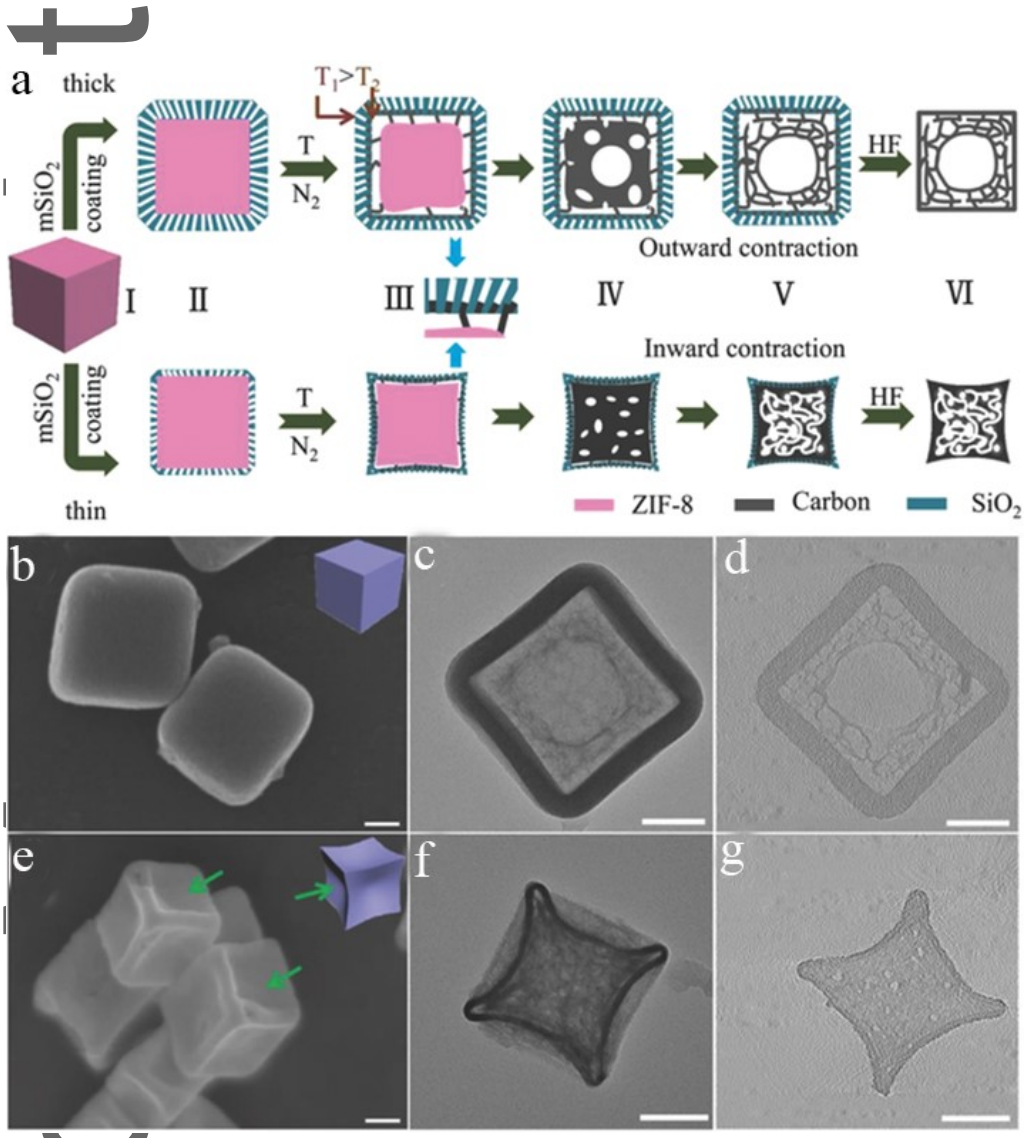

Figure 9. a) Schematic representation of the synthesis of HMCNCs and SMCNCs. b–g) FESEM images (b,e), TEM images (c,f), and ET slices (d,g) of carbon@mSiO_2-40 and carbon@mSiO_2-8, respectively. Scale bar is 100 nm. a–g) Reproduced with permission.[133] Copyright 2018, Wiley-VCH.

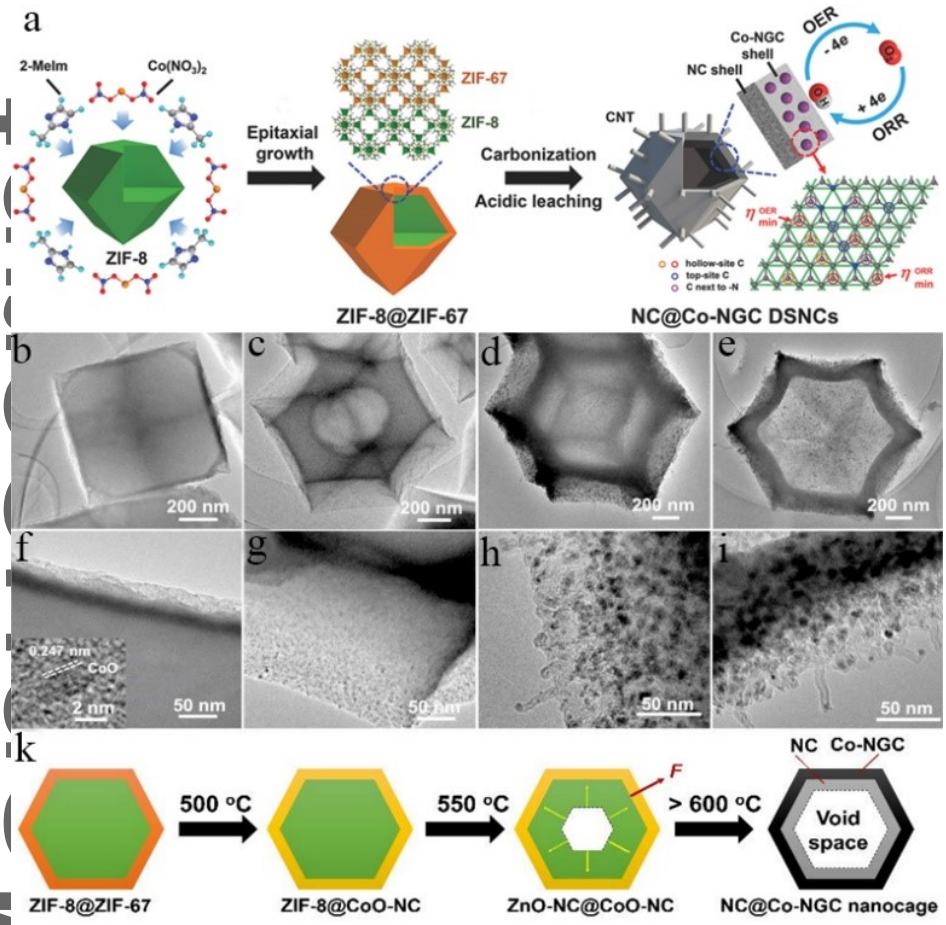

Figure 10. a) Schematic representation of the synthesis of NC@Co-NGC DSNCs. b–i) TEM images of core–shell ZIF-8@ZIF-67 nanoparticles annealed at 500 °C (b,f), 550 °C (c,g), 600 °C (d,h), and 800 °C (e,i). k) Schematic diagrams of the formation process of NC@Co-NGC DSNCs. a–k) Reproduced with permission.[185] Copyright 2017, Wiley-VCH.

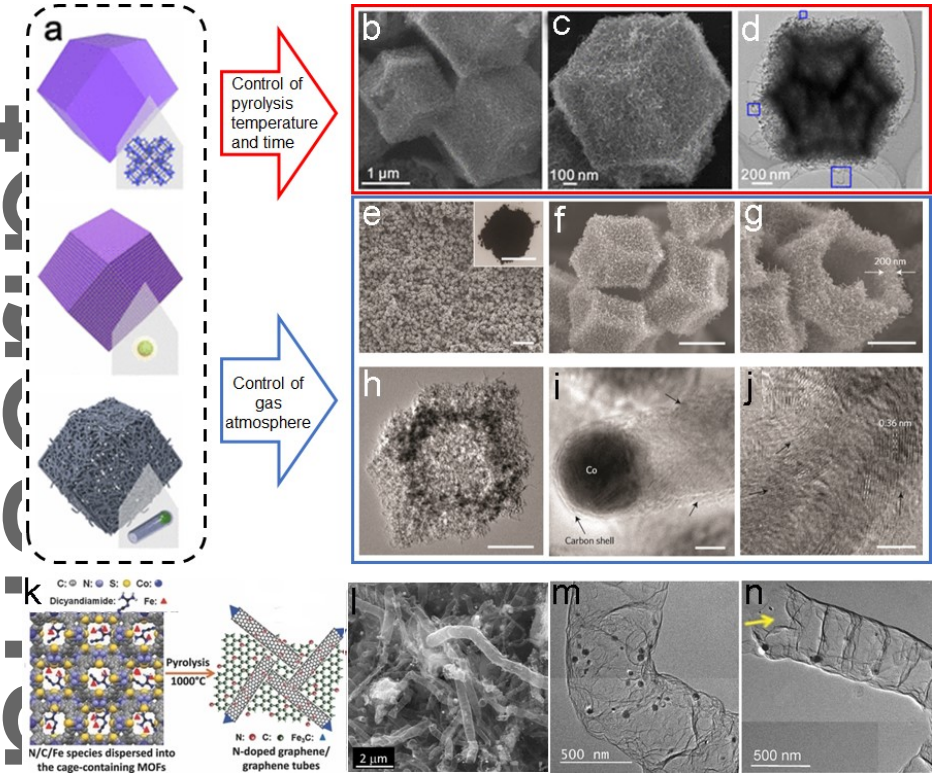

Figure 11. a) Schematic diagram of the synthesis of N-CNTs from ZIF-67. b−d) SEM, TEM, and HRTEM images of N-CNT-assembled hollow dodecahedra. a–d) Reproduced with permission.[191] Copyright 2017, American Chemical Society. e–j) FESEM images (e–g), TEM image (h), and HRTEM images (i,j) of as-prepared NCNTFs at 700 °C in the presence of H_2. In (j), 0.36 nm refers to the lattice spacing, indicated by the white dashed lines, on the carbon (002) plane. The arrows in (i) and (j) indicate the direction of the graphitic layers. The inset of (a) is a digital photo; the scale bar is 1 cm. Scale bars: 10 μm (e); 1 μm (f,g); 500 nm (h); 5 nm (i,j). e–j) Reproduced with permission.[193] Copyright 2016, Nature Publishing Group. k) Schematic illustration of the formation of graphene/graphene-tube nanocomposites at 1000 °C. l) SEM images of as-prepared N-GT pyrolysis at 1000 °C. m,n) TEM images of a typical graphene tube (m) and the open mouth of a graphene tube marked by a yellow arrow (n). k–n) Reproduced with permission.[190] Copyright 2014, Wiley-VCH.

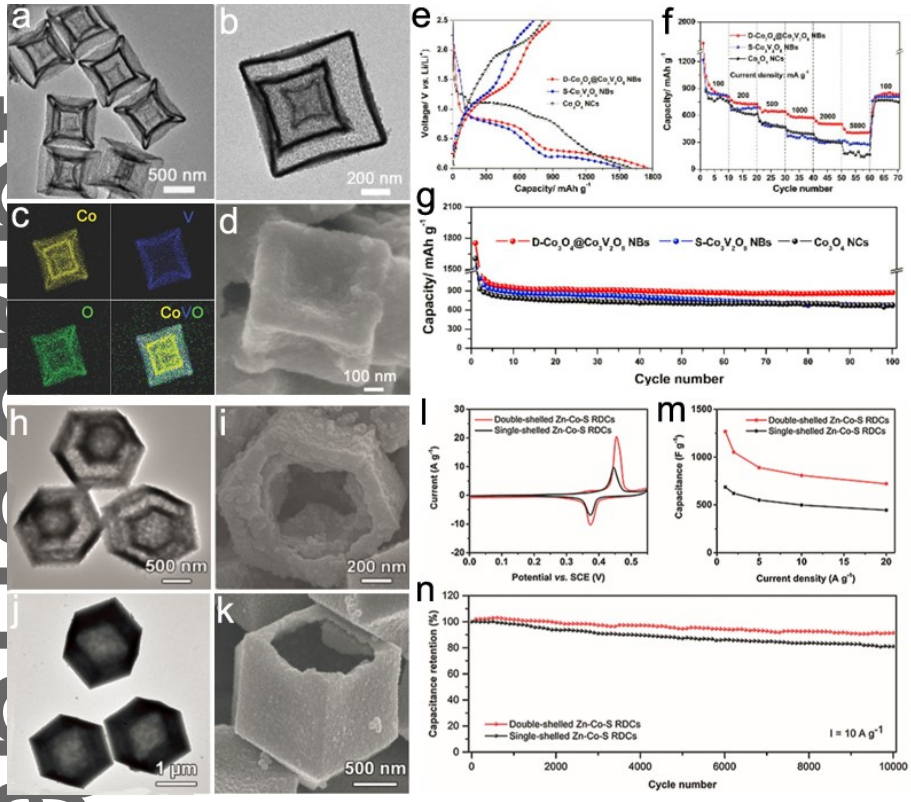

Figure 12. a,b) TEM images of as-prepared T-Co_3O_4@$Co_3V_2O_8$ nanoboxes. c) HAADF-STEM images of element mapping of typical nanoboxes. d) FESEM images of the T-Co_3O_4@$Co_3V_2O_8$ nanoboxes after a cycling test (100 cycles at 100 mA g^{-1}). e–g) Characterizations of the lithium-storage performance of the T-Co_3O_4@$Co_3V_2O_8$ nanoboxes: galvanostatic charge–discharge profiles at 100 mA g^{-1} (e), rate performance from 100 mAg^{-1} to 1000 mAg^{-1} (f), and cycling performance and the corresponding coulombic efficiency at 100 mA g^{-1} (g). a–g) Reproduced with permission.[148] Copyright 2018, Wiley-VCH. h–k) TEM images (h,j) and FESEM images (i,k) of as-prepared double-shelled Zn–Co–S RDCs (h,i) and single-shelled Zn–Co–S RDCs (j,k). l–n) Characterizations of the lithium-storage performance of double-shelled and single-shelled Zn–Co–S RDCs: CV curves at a weep rate of 1 mV s^{-1} (l), specific capacitance at different current densities (m), cycling performance at 10 A g^{-1} (n). h–n) Reproduced with permission.[201] Copyright 2017, Wiley-VCH.

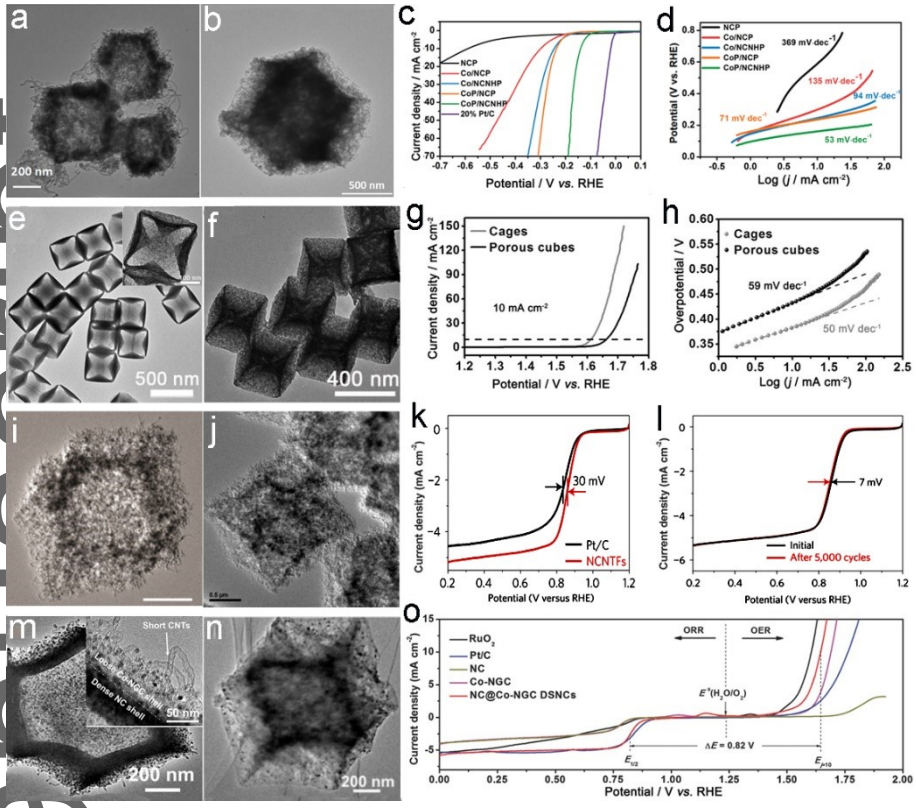

Figure 13. a,b) TEM images of the as-synthesized hollow CoP/NCNHP and CoP/NCP, respectively. c,d) LSV (c) and Tafel curves (d) of hollow CoP/CNT nanocomposites and the compared samples in 0.5 M H_2SO_4 for HER with a scan rate of 5 mV·s^{-1} at room temperature. a–d) Reproduced with permission.[183] Copyright 2018, American Chemical Society. e) TEM images of the as-prepared Ni–Co PBA cages and Ni–Co mixed-oxide cages (inset) with an average size of 400 nm. f) TEM images of Ni–Co oxide porous cubes. g,h) Polarization curves (g) and Tafel plots (h) of the Ni–Co mixed-oxide cages and porous cubes. e–h) Reproduced with permission.[125] Copyright 2016, Wiley-VCH. i) TEM images of as-prepared NCNTFs by annealing at 700 °C in Ar/H_2. j) TEM images of NCNTFs after a cycling test (5000 cycles at 100 mA g^{-1}). k) Comparison of Pt/C and NCNTFs in LSV curves (1600 r.p.m.). l) ORR polarization curves (1600 rpm) of NCNTFs before and after 5000 cycles. i–l) Reproduced with the permission.[193] Copyright 2016, Nature Publishing Group. m) TEM image of a single NC@Co–NGC nanocage; the partial magnification in the inset image presents a dual shell structure of an inner densely packed NC shell and an outer porous Co–NGC shell anchored with short CNTs. n) TEM images of ZIF-67-derived Co–NGC particles. o) Comparison of OER/ORR polarization curves of various catalysts tested in O_2-saturated 0.1 M KOH solution by using a three-electrode system. m–o) Reproduced with the permission.[185] Copyright 2017, Wiley-VCH.

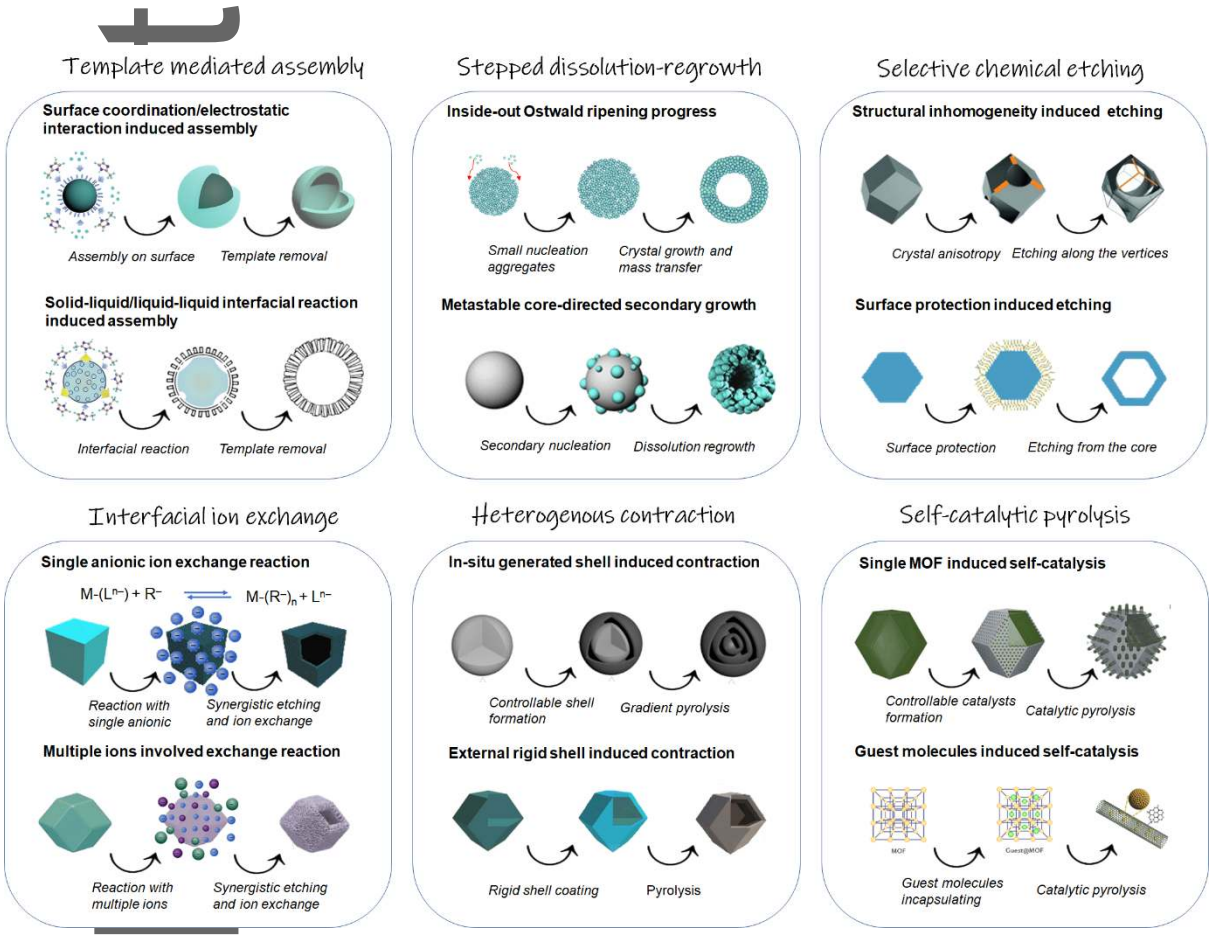

Figure 14. Summary of the synthetic strategies and their corresponding reaction mechanisms. There are fourteen types of reactions in six types of synthetic strategies. In the template mediated assembly, surface coordination/electrostatic interaction induced assembly and solid-liquid/liquid-liquid interfacial reaction induced assembly represent four types of reactions.

Table 1. Summary of various MOF-derived hollow structures prepared via conversion from hollow MOFs.

MOF-derived materials	MOF precursors	Synthesis strategies	Applications	Performance	Ref.
Single-holed hollow cobalt/N-doped carbon sphere	PS@ZIF-67	PVP-modified assembly of ZIF-67 on PS, direct carbonization in N_2	ORR	E_{onset}= 0.98 V vs. RHE; $E_{1/2}$ = 0.87 V vs. RHE; Tafel plots = 102 mV decade^{-1}	[77]
MoO_2/C nanotube	MoO_3@BMZIFs	MoO_3 nanorod as template, PVP modified assembly of Zn, Co-BMZIFs shell, annealing at 600 °C under N_2 atmosphere followed by washing with concentrated HCl	LIBs	Initial discharge capacity: 1652 mAhg^{-1}; CE: about 66%; reversible capacities: 810 mAhg^{-1} after 600 cycles at 1 Ag^{-1}	[80]
Hollow Cu/Co_3O_4 sphere	Hollow ZIF-67 spheres	CTAB micelle template, introducing transition Cu dopants, direct pyrolysis in air.	OER	$E_{10\ mA/cm^2}$ = 361 mV vs. RHE	[95]

Hierarchical CNT/Co_3O_4 microtubes	Tubular ZIF-67	PAN-$Co(Ac)_2$ nanofibers as precursors and template, dissolved PAN in DMF, heat treatment in Ar/H_2 and in air	LIBs	Initial discharge /charge specific capacities:1281 and 1840 mAh g^{-1}; CE: 100%; reversible capacity: 1281 $mAhg^{-1}$ after 200 cycles at 0.1 Ag^{-1}	[96]
CoS_2 nanobubble hollow prisms	ZIF-67 hollow prisms	Cobalt acetate hydroxide solid prisms as sacrifice template, sulfidation reaction in solution and then annealed at 350 °C in nitrogen for 2 h	LIBs	Initial discharge /charge specific capacities: 1542 /861 mAh g^{-1} CE: 100%; reversible capacity: 737 $mAhg^{-1}$ after 200 cycles at 0.2 Ag^{-1}	[97]
N-doped carbon nanopolyhedra	ZnO@bimetallic Zn/Co-ZIF nanopolyhedron	ZnO nanosphere as precursor and template, epitaxial growth of ZIF shell, high temperature carbonization and evaporation of ZnO	ORR	E_{onset} = 872 mV vs. RHE; $E_{1/2}$ = 0.796 V vs. RHE	[133]
Hollow ZnO microparticles	Hollow-Zn-BTC	Self-template formation, solvothermal reaction at 140 °C, thermal treatment in air	/	/	[64]
NiO/ZnO hollow sphere	Yolk–shelled Ni–Zn MOF microsphere	Solvothermal fabrication of yolk–shelled Ni–Zn MOF spherical particle , annealed in air at 500 °C	Supercapacitors	Specific capacitance: 497 Fg^{-1} at 1.3 Ag^{-1}; reversible capacity: 478 Fg^{-1} after 2000 cycles at 5.2 Ag^{-1}	[113]
Ni-decorated hollow molybdenum carbide structures	Mo-based POM-anion-incorporated Ni-MOF hollow sphere	Self-template formation, solvothermal reaction 180 °C for 28 h, annealing in N_2 at high temperature	HER	$E_{10\ mA/cm^2}$ = 123 mV vs. RHE; Tafel plots = 83 mV $decade^{-1}$	[119]
N/B co-doped hollow carbon	ZIF-8 dodecahedron	Tannic acid, 1,4-benzene diboronic acid as etching and doping source, carbonization in N_2	ORR	E_{onset}: −0.12 V vs. Ag/AgCl	[128]
Ni–Co-mixed oxide nanocage	Ni–Co PBA cubes	Modified precipitation synthesis of Ni–Co PBA cubes, etching in ammonia at room temperature, annealing at 350 for 2h	OER	$E_{10\ mA/cm^2}$ = 380 mV vs. RHE; Tafel slope = 50 mV $decade^{-1}$.	[125]

Table 2. Summary of various MOF-derived hollow structures prepared via conversion of solid MOF precursors.

MOF-derived hollow structures	Precursors	Synthesis strategies	Applications	Performance	Ref.
Fe_2O_3 microboxes; multicompositional microboxes	PB nanocube	NaOH solution, hydrothermal 80 °C for 10 h, $K_2MO_3 \cdot xH_2O$, $NaMO_2 \cdot xH_2O$ (M=Sn, Si, Ge, Al, B), Room temperature, 10 h	LIBs (Fe_2O_3/SnO_2 nanoboxes)	Initial discharge and charge: 1751 and 904 $mAhg^{-1}$; CE = 95%; reversible capacity: 500 $mAhg^{-1}$ after 100 cycles at 0.2 Ag^{-1}	[140]
Triple-shelled Co_3O_4@$Co_3V_2O_8$ nanoboxes	ZIF-67 nanocubes	Vanadium oxytriisopropoxide ethanol solution, solvothermal 120 °C for 2 h	LIBs	Reversible capacity: 948 $mAhg^{-1}$ after 100 cycles at 100 mAg^{-1};	[148]
NiS nanoframes	Ni-Co PBA nanocubes	Na_2S solution, hydrothermal, 100 °C for 6 h	Supercapacitor; HER	Specific capacitance: 711 Fg Ag^{-1} at 20 Ag^{-1}; reversible capacity: 1290 Fg^{-1} after 4000 cycles at 4 Ag^{-1}; HER: $E_{10\ mA/cm^2}$ =94 mV vs RHE;	[147]
Hollow $M_xCo_{3-x}S_4$, (M = Zn, Ni, and Cu) polyhedra	MCo-ZIFs polyhedra	Thioacetamide(TAA) ethanol solution, solvothermal, 120 °C for 4 h	HER ($Zn_{0.3}0Co_{2.70}S_4$)	$E_{10\ mA/cm^2}$ = 80 mV vs. RHE; Tafel plots ~ 47.5 mV $decade^{-1}$	[141]
Amorphous CoS nanocages	ZIF-67 polyhedra	TAA ethylene glycol solution, refluxing for 1 h	Supercapacitor	Specific capacitance: 932 Fg^{-1} at discharge 10 Ag^{-1}; reversible capacity: 822 Fg^{-1} after 1000 cycles at 10Ag^{-1}.	[195]
Hollow Co_3S_4@MoS_2 heterostructures	ZIF-67 polyhedrons	TAA and $Na_2MoO_4 \cdot 2H_2O$ mixed aqueous solution, hydrothermal 120 °C for 4 h followed by 200 °C for 8 h	OER	$E_{10\ mA/cm^2}$ = 330 mV vs. RHE; Tafel plots = 59 mV $decade^{-1}$	[143]
Complex CoS nanobubble cages	TiO_2/hexadecylamine @ZIF-67	Thioacetamide(TAA) ethanol solution, solvothermal, 120 °C for 4 h	Supercapacitor	Initial Specific capacitance: 1405 Fg^{-1} at discharge 4 Ag^{-1}; reversible capacity: 1290 Fg^{-1} after 4000 cycles at 4Ag^{-1}.	[196]

Hollow $NiCo_2O_4$ arrays	ZIF-67 nanoflakes	$Ni(NO_3)_2 \cdot 6H_2O$ ethanol solution, room temperature stirring for 15 min	OER	$E_{onset} \approx 1.49$ V; $E_{10\ mA/cm^2} = 1.57$ V vs. RHE; Tafel slope = 72 mV decade^{-1}	[155]
Ni–Co LDH nanocages	ZIF-67	$M(NO_3)_2$ ethanol solution (M= Mg, Co, Ni), refluxing for 1 h under stirring	Supercapacitor	Specific capacitances: 973 878 mAhg^{-1} at 8 Ag^{-1}; Reversible capacity: 878 mAhg^{-1} after 1000 cycles at 8 Ag^{-1};	[157]
Ni–Co–MoS_2 nanoboxes	Ni-Co PBA nanocubes	Ammonium thiomolybdate DMF solution, solvothermal 210 °C for 20 h	HER	$E_{10\ mA/cm^2} = 155$ mV vs. RHE; Tafel slope = 51 mV decade^{-1}	[153]
$CoMoO_4$–$Co(OH)_2$ nanocages, $CoWO_4$–$Co(OH)_2$ nanocages	ZIF-67 polyhedrons	Na_2MoO_4 and Na_2WO_4 water and ethanol mixture, refluxing at 82 °C for 2 h	OER (CoO–MoO_2 nanocages)	$E_{10\ mA/cm^2} = 312$ mV vs. RHE; Tafel slope = 69 mV decade^{-1}	[154]
Cu-Doped-$CoSe_2$ Microboxes	Co-Co PBA microcubes	Na_2SeO_3 and H_4N_2 aqueous solution, hydrothermal 160 °C for 8h	NaIBs	Initial charge capacity: 492 mAhg^{-1}; rate capacity: 398 mAhg^{-1} at 1 A g^{-1}	[197]
Fe_2O_3 microbox	PBA microcube	Directly annealing at 550 °C in air	LIBs	Reversible capacity: 945 mAhg^{-1} after 30 cycles at 1Ag^{-1}	[198]
Hollow Mesoporous Carbon Nanocubes	ZIF-8 nanocubes	Growth of a thick $mSiO_2$ layer, rigid-interface induced outward contraction.	LIBs	Rate capability: 455.1 mAhg^{-1} at 5.0 Ag^{-1}; reversible capacity: 812.6 mAhg^{-1} after 100 cycles at 0.2 A g^{-1}	[174]
CoP Nanoparticle-Embedded N-Doped Carbon Nanotube Hollow Polyhedron	Core–shell structured ZIF-8@ZIF-67	Controlled pyrolysis at 920 °C in flowing Ar – oxidation at 350 °C in Ar for 4h –phosphidation by annealing with NaH_2PO_2 at 300 °C in Ar flow.	HER	$E_{10\ mA/cm^2} = 140$ mV vs. RHE; Tafel slope = 53 mV decade^{-1}	[183]
$Fe_{0.3}Co_{0.7}$ Alloy/Nitrogen-Doped Carbon Cages	ZIF-8@FeOOH/ZIF-67 core–shelled hybrid	Direct annealing in N_2 through a confined pyrolysis of "MOF-in-MOF hybrid" process	ORR	$E_{1/2} = 0.88$ V vs. RHE; Tafel slope = 79 mV decade^{-1}	[184]
Double-shelled NC@Co-NGC nanocages	Core–shell structured ZIF-8@ZIF-67	Controlled pyrolysis in flowing N_2 at 800 °C, followed by acid washing, rigid-interface induced outward contraction.	ORR; OER	ORR: $E_{onset} \approx 0.92$ V vs. RHE; $E_{1/2} = 0.82$ V vs. RHE; Tafel slope = 51 mV decade^{-1}; OER: $E_{10\ mA/cm^2} = 1.64$ V vs. RHE; Tafel slope = 91 mV decade^{-1}	[185]
Core–Shell $ZnCo_S$@Co_9S_8/N-doped Carbon	ZIF-67/ZIF-8@ZIF-67 Bimetal MOF	Thioacetamide, refluxing at 90 ˚C for 15 min, annealing at 700 ˚C in nitrogen flow for 3h.	LIBs	Initial discharge capacity: 2895 mAhg^{-1} at 100 mA g^{-1}, reversible capacity: 1814 mAhg^{-1} after 500 cycles at 0.5 A g^{-1}	[152]
Nitrogen-doped CNT-assembled hollow structures	ZIF-67 polyhedrons	Controlled low temperature pyrolysis, in-situ self-catalytic growth of N-CNT	ORR (N-CNTs-650)	CV peak potential: 0.87 V; $E_{1/2} = 0.85$ V vs. RHE; long-term stability: 95% current retention after 40000 s	[191]
Nitrogen-doped CNT-assembled hollow structures	ZIF-67 polyhedrons	Controlled pyrolysis in reductive gas, in-situ self-catalytic growth of N-CNT	ORR; OER	ORR: $E_{1/2} = 0.87$ V vs. RHE; Tafel slope ~ 64mVdecade^{-1}; OER: $E_{10\ mA/cm^2} = 1.6$ V vs. RHE; Tafel slope = 93 mV decade^{-1}	[193]
N-doped graphene/graphene tubes	A kind of N-Fe-MOF with dicyandiamide and Iron acetate encapsulated	Annealing at 1000 ˚C in N_2 atmosphere for 1 h and leaching in 0.5 M H_2SO_4	ORR	ORR: $E_{1/2} = 0.88$ V vs. RHE	[190]
Bamboo-like nitrogen-doped graphene tubes (N-GTs)	MIL-100 with dicyandiamide and Iron acetate encapsulated	Annealing at 1000 °C in an N_2 atmosphere for 1 h and leaching in 0.5 M H_2SO_4 at 80 °C for 8 h	ORR	ORR: $E_{1/2} = 0.88$ V vs. RHE (20 wt% Pt/N-GT catalysts)	[194]

Ze-Xing Cai received his Ph.D. degree from Huazhong University of Science and Technology (HUST) in 2017. Since then, he started his postdoctoral work with Prof. Yusuke Yamauchi supported by a JSPS Postdoctoral Fellowship at the National Institute for Materials Science (NIMS).

Zhong-Li Wang received his Ph.D. degree from Changchun Institute of Applied Chemistry (CIAC), Chinese Academy of Science (CAS) in 2010. After his graduation, he worked as an

assistant professor at CIAC. He became an associate professor in 2012 at CIAC. In 2015, he joined Prof. Yusuke Yamauchi's group with JSPS Postdoctoral Fellowship in NIMS, Japan. In 2018, he became a NIMS postdoctoral researcher. His current research interests are advanced carbon and inorganic functional materials for electrochemical energy storage and conversion.

Yusuke Yamauchi received his bachelor's degree (2003), master's degree (2004), and Ph.D. degree (2007) from Waseda University, Japan. After receiving his Ph.D., he joined NIMS to start his own research group. From 2018, he joined the University of Queensland (Australia) as a full-time professor. He concurrently serves as an honorary group leader of NIMS and a visiting professor at several universities.

Recent developments of controlled synthesis of hollow-structured functional materials by using metal–organic framework (MOFs) as precursors are summarized, along with their promising applications in electrochemical energy storage and conversion.

((ToC keyword) Metal–Organic Framework Precursors

Z.-X. Cai, Z.-L. Wang,* J. Kim, Y. Yamauchi*

Hollow Functional Materials Derived from Metal–Organic Frameworks: Synthetic Strategies, Conversion Mechanisms and Electrochemical Applications